Large Strain Finite Element Analysis of Spinodal Shell Structures

Colin Gabriel Wilson

A thesis
submitted in partial fulfillment of the
requirements for the degree of

Master of Science

University of Washington

2023

Reading Committee:
Lucas Meza, Chair
Mohammad Malakooti
Marco Salviato

Program Authorized to Offer Degree:
Mechanical Engineering

University of Washington

Abstract

Large Strain Finite Element Analysis of Spinodal Shell Structures

Colin Gabriel Wilson

Chair of the Supervisory Committee:
Assistant Professor Lucas Meza
Mechanical Engineering

Nanoarchitected materials combine architecture properties with nano-scale size effects such as increased tensile strength, but often suffer from localized failure and low mechanical efficiency. Architectures derived from spinodal decomposition have promising material properties due to their continuous doubly curved surfaces with minimal stress concentrations.

In this work, finite element analysis was used to model spinodal shell structures, allowing the study of the architecture properties and inspection into the interior of the structure to allow a better understanding of the nanomaterial behavior. Isotropic, lamellar, columnar, gradient, and bioinspired conch architectures were simulated up to 0.5 strain at relative densities ($\bar{\rho}$) between 0.001 and 0.01, in order to match the conditions of nanoindenter tests of the same structures.

The simulations provided results close to the experiments in elastic stiffness and plateau stress. Each of the architectures scales elastic modulus and yield strength proportional to $\bar{\rho}^2$. The experiments showed extensive localization effects, especially localized buckling at the bottom layer and localized fracture in the top layer, but the simulations showed only localized auxetic behavior in the middle of the structures. Strain localization was observed in the gradient structures, as the changing anisotropy encouraged strain to localize to each layer, but this strain did not cause localized failure. The stress state within the structures showed stress concentrations occur in areas of connections between layers, but the structures

may have additional load paths that can be activated when the highly stressed areas buckle or fracture, preventing catastrophic failure and enabling recovery.

This work shows the benefits of the spinodal architecture in eliminating localized deformation, controlling strain patterns through anisotropic and gradient architecture designs.

TABLE OF CONTENTS

LIST OF FIGURES

Figure Number Page

LIST OF TABLES

Table Number Page

ACKNOWLEDGMENTS

S.D.G.

I want to start off by saying that I'm so grateful for the opportunity to have gotten to this point. In the past I had thought that it might be nice to get more education, but I hadn't imagined that a pandemic might get me to go in this direction, and I also hadn't thought I would be writing a thesis, but that was sort of accidentally dropped in my lap by my own errors. That being said, it's a privilege to be able to finish my work like this and have something great to show for my time spent during my degree–the biggest paper I've ever written.

Thanks to my wonderful wife Jiayun for her patience with me as I have gone through my degree and thesis writing. I would like to think that the last 2.5 years have made me more available for the family, but I know that hasn't always been the case, especially in the last few months of intense thesis work. I'm grateful for her support through this and I couldn't have done it alone. And of course Calvin and Allen, who always help distract me from my work with exciting artwork and construction projects and important things to tell me. And I have never ending gratitude to my parents, who, aside from everything they have done for me throughout my life, have always been there for me as I've worked through my classes and projects, especially in 2020 when I started and we still did not have childcare for Calvin during the day.

Thanks to Professor Meza for bringing me into the lab and working with me so much. I wonder sometimes if I have taken too long in my project and need too much help in understanding the basics of nanomaterials, but I always feel welcome and encouraged when we meet.

Thanks to Nishita for providing all the experimental data in this thesis which I contributed relatively little to producing, particularly the SEM images used in the thesis. And also for giving me some of my only experiences in conducting experiments such as by breaking alumina with my camp stove in the fume hood.

Thanks to Kush for his help with so much of the technology I've needed for my work. We've been working through some of the same things and it's been great to have a partner in this learning process. And I appreciate all the help with Abaqus details, and of course fixing the lab computer, which I am capable of doing, but had no time for.

Chapter 1

INTRODUCTION AND BACKGROUND

1.1 Architected Materials

Materials research has traditionally relied on empirical trial and error methods to create materials with optimized properties, often with new chemical combinations of materials, and new methods of heat treatment or cold-working. These processes have been fully developed, so they can produce only slight improvements compared to the existing materials. Architected materials offer an additional method for improving properties, using a combination of different materials or voids to create a material with different properties. The goal of developing these new materials is to expand the material property space, which represents the combination of all material properties, and new materials are sought which fill new areas of the property space, as shown in Figure 1.1. Composite materials and foams are both classes of architected materials since composites are made up of multiple materials, and foams are made up of solid materials combined with voids, both in ways that provide some improvement to properties compared to constituent materials[1].

Research into different lattice architectures has provided a significant body of data into properties of architected materials at different scales and relative densities[2, 3, 4, 5, 6, 7]. One of the key benefits found in the study of lattice architectures is that of recovery and resilience. Despite the damage experienced during compression testing, lattices are often able to recover to their original shape, continuing to carry load for repeated cycles, a feature that is enabled by buckling in the lattice beams. When damage or plasticity occurs, the properties will be substantially degraded on subsequent cycles, but the ability to carry load, absorb energy, and maintain its original shape is largely maintained. In addition, tests show a hysteresis in the stress-strain curve between the compression and the recovery, and this difference represents the energy absorbed during the test [2, 3, 4]. The high resilience and energy absorption in such metamaterials leads to applications in space debris impact protection and ballistic defence[8].

Lattices have different mechanical behaviors which drive performance characteristics, including material fracture, Euler buckling, and shell buckling in hollow lattices [3]. Though solid lattices are mechanically efficient, at low relative density they tend to buckle because buckling strength reduces quickly at low relative density and Euler buckling becomes the dominant failure mode[9].Hollow lattices reduce the buckling threshold to a lower relative density, but they often perform poorly due to the lack of stiffness of the connecting nodes. Were it possible to increase the stiffness of the nodes during manufacturing, they would have significantly higher strength[10]. They are also highly sensitive to imperfections, especially imperfections introduced by the manufacturing process. One study (Meza et al.) found the effective stiffness of hollow alumina beams in a lattice was reduced by 70% due to waviness of the surface caused by vibration during manufacturing[4].

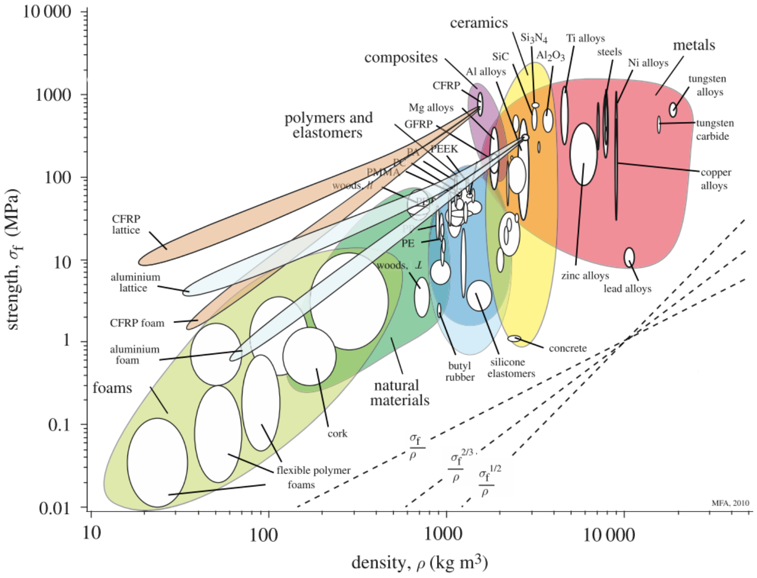

Figure 1.1: A representation of the material property space referred to as an Ashby chart, showing density vs. strength. A target for expansion of the material property space in this representation is the blank space up and to the left of the currently shown materials, since this would result in higher strength and lower density, both desirable traits for most material applications. Image from [1]

The weaknesses of lattice architectures have led to new architectures being used in metamaterial research, especially continuous, smoothly curved shell architectures. Shells are thin structures which transmit load primarily through membrane stresses[11]. One set of shell designs is the triply periodic minimal surfaces (TPMS), which have constant zero mean curvature on the entire surface, with double curvature, in which the two principal curvatures are non-zero. This constant curvature means that it does not have the stress concentrations seen at the nodes of hollow lattices[12, 13]. Double curvature has proven to increase stiffness of structures by increasing the energy requirement to undergo bending, so that loads tend to be carried in tension and compression[14].

TPMS inspired architectures have been used to create shell-based architected materials. Due to their continuous nature, and lacking the nodes of lattices, shells made from these surfaces do not suffer from stress concentrations which cause premature structural failure and low stiffness at low relative density[15]. TPMS-inspired architectures, such as a Schoen F-RD type surface, showed substantially higher energy absorption compared to a truss lattice [16]. At high relative densities, shell architectures can be quite stiff, reaching 70% of the Hashin-Shtrikman bound, a theoretical limit for material stiffness[17]. Like lattices, they can also to be sensitive to imperfections, such as the surface roughness introduced by 3D printing, which can cause premature buckling[18]. Due to their periodic nature, such shell structures tend to collapse layer by layer or with the formation of shear bands. This localized collapse results in softening, seen as negative stiffness in the stress-strain curve[13, 18, 17, 16].

1.2 Spinodal Shell Materials and Spinodal Decomposition

The spinodal interface surface, defined by spinodal decomposition, is doubly curved with many features similar to TPMS surfaces[13]. Prior work has shown the behavior of spinodal materials with small strain, showing the the elastic modulus for different material architectures and relative densities[19]. Spinodal shell structures have shown low sensitivity to imperfections compared to other shell structures, and they tend to perform much better than lattices and other shell materials at relative density below 1%[20]. In experimental tests, they have shown excellent recovery in thin walled shells, but typically see extensive

Figure 1.2: The process of spinodal composition, where the two phases, shown as black and white, coalesce together into larger and larger feature sizes. Image courtesy Yonatan Oren, from Wikimedia.

fracture damage in thicker shells. Similar to lattices, in repeated cycling, there is some loss in properties with successive cycles, but some structural integrity is maintained after the initial compression[15]. The behavior of solid spinodal materials has also been studied, with glassy carbon spinodal structures showing high stiffness and energy absorption[21].

Spinodal decomposition is a process by which dissimilar materials in a solid solution separate into multiple phases, in order to reach a more energetically optimized state[22]. Each phase of the spinodally decomposed material is bicontinuous and following a tortuous path. As time progresses, the feature size becomes coarser as the phases concentrate together more and more, as shown in Figure 1.2. A spinodal metamaterial can be created by removing one of the phases produced during spinodal decomposition, leaving the remaining phase as a porous, continuous material. While the spinodal decomposition process has been understood for some time, the usefulness of this process for creating metamaterials was not found until much later[15, 19, 21, 20].

Spinodal decomposition is modeled using the Cahn-Hilliard equation. In describing the natural process, this equation produces an isotropic material, but it has been modified to allow for preferential directions for the interface surface between the phases. This has been used to test the impacts of anisotropy on nano-scale architectures. The anisotropic equation is[23, 24, 25]

$$\frac{\partial \varphi}{\partial t} = M\nabla \cdot \left(\epsilon_{\varphi}\nabla\left(\frac{\gamma(\mathbf{n})}{\epsilon}\varphi\left(\varphi^2 - \frac{3}{2}\varphi + \frac{1}{2}\right) - \epsilon\nabla \cdot (\gamma(\mathbf{n})\nabla\varphi + |\nabla\varphi|(\mathbf{I} - \mathbf{n}\otimes\mathbf{n})\nabla_{\mathbf{n}}\gamma(\mathbf{n}))\right)\right) \tag{1.1}$$

where φ represents the concentration of one phase, M represents the mobility constant, ϵ represents the length scale, and $\mathbf{n}$ represents the concentration gradient unit vector. The difference between isotropic and anisotropic equations lie in the $\gamma(\mathbf{n})$ and ϵ_{φ} terms. In the conventional formulation of the equation, ϵ_{φ} equals ϵ, but for the anisotropic version it is made a function of φ to increase mobility at the phase interface, and is equal to $\varphi(1-\varphi)/2$. $\gamma(\mathbf{n})$ has the effect of reducing free energy when a surface is aligned with a preferential direction, and is defined as

$$\gamma(\mathbf{n}) = 1 - \sum_{i=1}^{\alpha} a_i(\mathbf{n}\cdot\mathbf{m}_i)^4\mathcal{H}(\mathbf{n}\cdot\mathbf{m}_i) \tag{1.2}$$

where α is the number of preferential directions, a_i is the degree of anisotropy, m_i is the set of preferential directions, and $\mathcal{H}$ represents the heaviside step function. When α is 0, with no preferential directions, the system is isotropic, and $\gamma(\mathbf{n})$ equals 1. When anisotropy is introduced, the dot product and a_i coefficients are nonzero and $\gamma(\mathbf{n})$ is not constant, so that the equation prefers energy minima that develop in the direction of $\mathbf{m}_i$. This equation does not have a closed-form solution and is solved numerically, which is computationally intensive and is not practical for studying large numbers of structures. The solution produces a grid of values between 0 and 1 representing the phase volume fraction, with a value of 0.5 representing the phase interface.

A similar topology can be created which is useful for approximating the Cahn-Hilliard solution while requiring less computation time. This spinodoid is a stochastic structure which can produce similar architectures to both isotropic and anisotropic spinodal materials, by generating a Gaussian Random Field (GRF) using a large number of sine waves. Random vectors $\mathbf{n}_i$ are generated, and those within a specified angle of the preferential direction vectors are kept and used to generate the GRF φ according to

$$\varphi(\mathbf{x}) = \sqrt{\frac{2}{N}} \sum_{i=1}^{N} \cos(\beta \mathbf{n}_i \cdot \mathbf{x} + \gamma_i) \tag{1.3}$$

where N is the number of vectors, β is the wave number chosen in the input parameters, $\mathbf{x}$ represents the location in cartesian space, and γ_i is the randomly generated wave phase[19, 26]. The preferential directions have a shorter wavelength resulting in a smaller feature size compared to other directions. By using this periodic function, regions of each phase are generated, with a feature size determined by β, so that the result is like a spinodal with two bicontinuous phases. The full formulation is described in detail in Appendix A.

Spinodal decomposition may be used as a method to reduce the cost of production of advanced materials. For example, a mixture of a two part epoxy with polyethylene glycol (PEG) initiates spinodal decomposition where one phase is the hardened epoxy and the other is PEG. Because PEG is soluble in water, it can be easily removed creating a cellular polymer structure[15, 27]. Another step may be taken by coating the polymer structure with alumina using atomic layer deposition (ALD). After coating the structure, the coated cellular polymer can be removed creating a hollow shell structure[15]. While many metamaterials require slow 3D printing techniques to manufacture, using this self-assembly technique could allow higher amounts of material to be made leading to possible industrial applications. With self-assembly, 3D printing induced imperfections are eliminated, potentially allowing higher performance. It is still useful to use 3D printing to create test models so that the identical model can be used to create a finite element analysis (FEA) model. This introduces some imperfections into the experiments, but allows experiments and FEA simulations to be run on identical structures.

1.3 Localization of Deformation and Damage

The failure mode of most materials involves some sort of localization, in which material damage, such as fracture or plastic deformation, is unequally distributed throughout the structure, with critical loads reached only in some parts of the structure. This can be observed in the shear bands found in conventional tensile test samples caused by plastic deformation[28]. Porous metamaterials show localization effects, notably in stretch-dominated materials, which tend to have post-yield softening when failure occurs, and can lead to catastrophic failure[29]. Softening of one weak part of the structure, by buckling or fracture, causes nearby areas to also fail, causing shear bands or entire layers to collapse. Post-collapse softening may occur repeatedly when a structure has periodic layers[9]. In order to mitigate the risk of catastrophic collapse of structures, designs must introduce large factors of safety introducing substantial extra material, in order to ensure that the structural behavior remains in the stable linear elastic region[28].

Porous materials can be modeled as having post-yield hardening, followed by softening, and then continued hardening, although an ideal foam would be perfectly plastic during the hardening phase, as shown in Figure 1.3. The softening is caused by buckling, which reduces the load in the buckled members and redistributes load elsewhere in the structure. The final hardening represents densification of the material, in which material self-contact occurs providing additional load paths and thus an increase in stiffness[31, 30]. In layer-by-layer collapse, each collapsed region will undergo this hardening-softening-hardening process until the stress reaches the previous peak and the other regions begin to increase stress again.

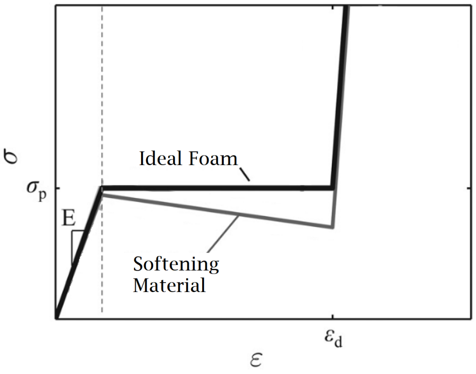

Figure 1.3: An ideal foam has no softening at σ_p (negative slope), but typical porous materials will see a negative slope causing a reduction in stress before seeing increased stress with densification at ϵ_d. Image from Hutchens et al.[30].

The stochastic nature of spinodal architectures opens the possibility of eliminating certain localization effects seen in periodic structures, such as layer collapse and shear banding. Careful control of the load path in a lightweight material has demonstrated a reduced tendency to form shear bands. This can be done by creating discontinuous load paths, rather than direct connections of areas under compressive loading[28, 32]. Spinodal materials have been tested for compression strength, and localization of damage and deformation has been observed in these tests[15]. FEA simulations have typically been limited to very small strains, showing the initial stiffness without exploring post-buckling behavior, or with architectural parameters putting the material response into yielding rather than buckling[20].

Localization may be quantified using a delocalization coefficient to show the differences in performance between various architectures. This is defined as

$$\eta_d = 1 - \frac{std(\epsilon_v)}{std_{max}} \tag{1.4}$$

where std_{max} is the maximum expected standard deviation and ϵ_v is volumetric strain ($\epsilon_v = \epsilon_x + \epsilon_y + \epsilon_z$; Bauer et al. used unit cell area). A coefficient value of 1 represents full delocalization, or homogeneous strain, indicating high structural efficiency and potentially a higher performance material. The use of this delocalization coefficient with lattice structures showed that with certain lattice architectures, localization was largely eliminated[28].

1.4 Nanomaterial Properties

The architecture of a metamaterial heavily influences its properties, especially the stiffness, anisotropy, and recoverability. These properties can be studied at a macro scale, where the material properties are well understood. An architected nanomaterial allows the inclusion of nano-scale size effects which can improve material properties. As the size of critical architecture features is reduced, the number of flaws in the material will be reduced[9]. This is shown in the equation for fracture strength of a thin shell

$$\sigma^f \propto \left(\frac{1}{t}\right)^{(1/m)} \tag{1.5}$$

with t as the shell thickness and m as the Weibull modulus. As thickness is reduced, the fracture strength will increase, so that material strength is increased at nano-scale. This is particularly notable with ceramics, which have no plasticity to increase material toughness and see a wide distribution of failure strengths, resulting in a small Weibull modulus which leads to substantial improvement in strength as thickness decreases. This increase in strength is caused by a reduction in flaws, and will eventually reach a material limiting strength, shown in Figure 1.4, which represents the atomic bond strength[33]. The increased material strength combined with architecture allows ceramics to buckle rather than break, allowing recoverability even when some parts of the structure fracture[9].

Crack propagation is also effected by nano-scale size effects. With sufficiently thin curved shell walls, cracks will form in ways that prevent their propagation through the structure. This results in thinner shells experiencing buckling and recovery, while thicker shells see catastrophic fracture failure[21].

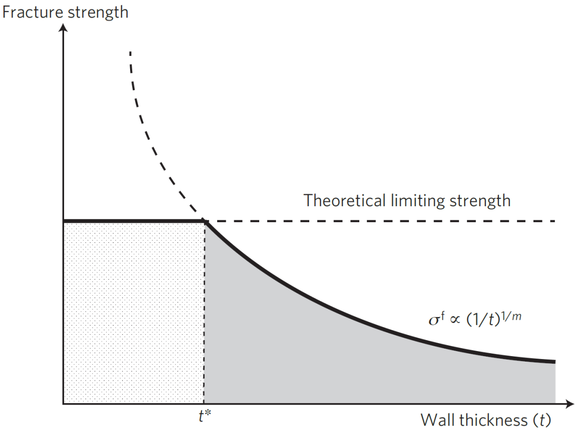

Figure 1.4: Reduction in shell wall thickness results in an increase in fracture strength, up to a limiting strength defined by atomic bond strength. Image from Jang et al.[33].

1.5 Natural Materials

Many natural materials provide examples of architected materials which can be used directly or as inspiration for new architected materials. Natural architected materials include the conch shell and the cuttlefish bone, shown in Figure 1.5. A conch shell microarchitecture serves to increase fracture toughness of the conch shell by 10000 times compared to the brittle ceramic aragonite ($CaCO_3$) from which it is composed. This toughness is caused in part by the delocalization of cracking, in which cracks in the shell take multiple branching paths which increases the energy absorption[34]. This architecture has been used in bioinspired materials

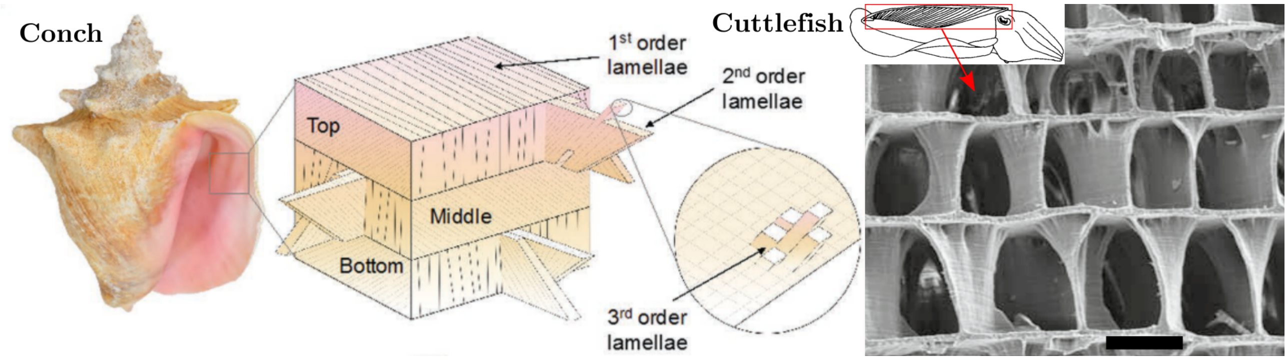

Figure 1.5: A conch shell is primarily made from aragonite, with layers of aragonite held together with an organic binder. It is structured in 3 macroscopic layers, each of which are made up of multiple orders of lamellae, with the 2nd order lamellae oriented at 45 degrees to the outside surfaces[34]. The cuttlefish bone provides structure and aids in buoyancy, and has a porous and periodic structure (scale bar 0.1mm). Images from Gu et al.[35] and Cadman et al. [36]

designed to increase fracture toughness by similarly deflecting cracks to increase toughness[35]. The cuttlefish bone is a highly anisotropic, columnar architecture also made from aragonite. It is periodic, porous and has high bending stiffness and compressive strength, and functions as both skeleton structure and buoyancy tank allowing the cuttlefish to pump water in and out of the bone to maintain its or change its position[36, 37]. The natural architecture has been used to create biocompatible scaffolds[38] and has been studied as inspiration for bioinspired cellular materials[36].

1.6 Cellular Material Scaling and Properties

As relative density is reduced in a material, properties such as elastic modulus and yield or tensile strength are reduced as well. The theoretical limit on elastic modulus in a material is the Voigt bound, or the rule of mixtures, which is the elastic modulus of the solid multiplied by the relative density, which is defined as $\bar{\rho} = \rho/\rho_s$ where ρ is the effective density, and ρ_s is the density of the solid material. A slightly lower limit is the Hashin-Shtrikman bound, which is a function of relative density and elastic, shear, and bulk moduli[39]. Real material properties are lower than these due to architectural and material limitations.Elastic modulus and yield stress are often suggested to scale according to a function of relative density

$$\frac{E}{E_s} = B\bar{\rho}^m, \frac{\sigma_y}{\sigma_{ys}} = C\bar{\rho}^n \tag{1.6}$$

where B and C are proportionality constants, m and n are scaling exponents, and E_s and σ_{ys} are the elastic modulus and yield stress of the solid material, respectively[29]. A scaling exponent of 1 would indicate no loss of specific performance with a reduction of relative density. Architectures are often categorized as stretching and bending dominated architectures, depending on whether loads are carried in tension and compression or bending. An ideal material scales linearly, indicating no loss of specific performance with a reduction of relative density ($m = n = 1$), while a theoretical bending-dominated architecture may see values of $m = 2$ and $n = 1.5$[9, 29]. The validity of the scaling equations, and the categorization of materials as stretching or bending dominated is in question, since the behavior of actual structures are much more complicated than a simple truss structure. However, they remain a useful metric for understanding the relative performance of lightweight materials[40].

The study of material property scaling is focused on producing lightweight materials with better material properties, such as higher elastic modulus and strength. Hollow lattices materials have shown good properties at low relative density[4], but conventional lightweight materials, such as foams, perform poorly[9]. Aerogels perform worse than conventional foams, due to poor mechanical efficiency[41]. Solid spinodal structures are difficult to test at low relative density, but spinodal shell materials at low density have performed similarly to other lightweight materials at low relative density[20, 15], however study of spinodal architectures tends to focus on the benefits of its stochastic features and self-assembly.

1.7 Experimental Setup

The experimental data used in this work was collected using a set of samples built using the same mesh developed for the FEA simulations. Test samples were made by printing a spinodal scaffold structure using 2-photon polymerization, with a size of 125μm on each side. Each scaffold was coated with alumina (Al_2O_3) using ALD, with coating thicknesses of 10nm, 40nm, and 80nm. The top surface of each sample was damaged using a focused ion beam (FIB) to allow for the polymer to be etched from the inside of the structure. The scaffold was removed in an inductive oxygen plasma etcher, leaving behind the alumina shell without damage. Compression tests were conducted using an Alemnis In-Situ Nanoindenter, completing a full cycle of displacement controlled compression up to 0.5 strain at 0.01 strain rate, followed by recovery back to 0 strain at the same strain rate. At each increment of 0.1 strain, the displacement was pulled back slightly to determine the local recovery modulus. Load and displacement data are generated by the nanoindenter, and videos are available from an SEM during the entire test.

1.8 Research Goals

This research is focused on understanding the mechanical behavior of spinodal shell architectures through FEA simulations, using different architectures to gain a broad understanding of anisotropic and gradient spinodal architectures. This includes using the natural conch shell architecture to create a bioinspired gradient material to study if a conch shell inspired architecture can also mitigate damage propagation. After validating the FEA model, the material properties for the metamaterial will be calculated, including elastic modulus, poisson's ratio, and yield stress.

There are several important aspect of nanoarchitected materials which can be studied using FEA. First, the study of localization is useful for developing efficient architected materials. Using experiments to observe localization may cause the results to be affected by manufacturing defects and material fracture which do not represent the properties of the material architecture. This will also help in understanding the impact of anisotropic and functionally graded spinodal architectures.

FEA simulations allow investigation to the behavior of internal parts of the metamaterial which cannot be observed with SEM imagery, including a full stress and strain field and buckling modes. This may be used to discover the features in the structures which are prone to damage or may contribute to a reduction in performance of the architecture.

The simulations will provide a simplified model of the entire material and architecture system allowing investigation into each separately. Discrepancies between simulation and experiment provide new insights into the behavior of the nanomaterials and a better understanding of the process for manufacturing and testing nanomaterial samples.

Chapter 2

STRUCTURE DEFINITION AND MESH GENERATION

2.1 Architecture Descriptions

In this study, spinodal and spinodoid shell architectures were used for experimental testing and numerical simulations. The architectures designed for this study were isotropic (iso), lamellar (lam), columnar (col), and gradient (grad) spinodal architectures and a bioinspired spinodoid conch architecture, all shown in Figure 2.1. The architectures are designed to be equal in surface area, so that the relative density should be similar when using the same ALD coating thickness.

The isotropic structure represents the natural geometry that emerges from spinodal decomposition processes, with no preferential anisotropic direction. The surface maintains near constant curvature, and is highly interconnected. The columnar and lamellar structures each use a single preferential direction vector, with the difference between the structures being only the orientation of the testing. The curvature of these structures is not constant like the isotropic, as the preferential direction has created many flat lamellae oriented perpendicular to the direction vector. The gradient architecture uses a lamellar architecture for its base and top surfaces, with a columnar band in the middle. This design is intended to allow use as a surface coating, where the lamella on the bottom would provide a suitable surface for attachment to a substrate, and the lamella on the top provide a stronger barrier to high air pressure than would a columnar architecture.

The conch mesh is a spinodoid mesh generated with lamellae inclined 45 degrees and built in 8 layers with the lamellae pointed into 4 directions, forming a helicoidal path inspired by the conch shell architecture. This structure uses a different preferential direction vector for each layer, which like the spinodal lamellar architecture produces lamellae perpendicular to

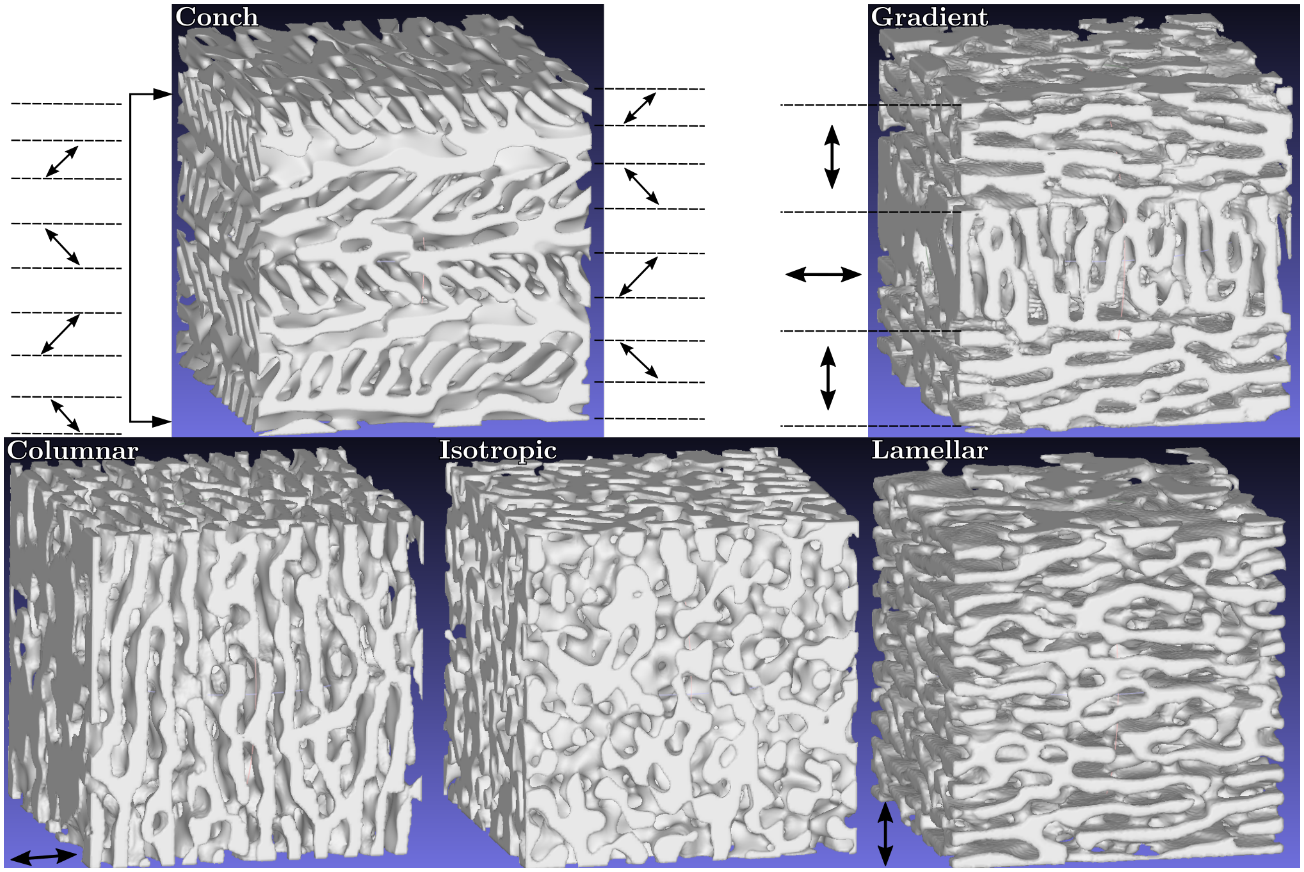

Figure 2.1: The different tested architectures. The arrows show the orientation of the preferred directions ($\mathbf{m}_i$) used by the Cahn-Hilliard equation and spinodoid function.

the preferential vector.

These architectures were selected to determine if the gradient architectures (conch and spinodal gradient) can be used to inhibit the localization which is problematic in architected materials, especially the formation of shear bands.

2.2 Mesh Generation

2.2.1 Mesh Creation

Both the Cahn-Hilliard equation and the spinodoid code produce a 3D grid of values from which a phase boundary can be estimated. Here we use the MATLAB isosurface and isocaps functions generate a mesh of triangular elements from the 3D grid, creating elements at the estimated location of the phase boundary, and closing the exterior surface to represent the inside and outside of the material. This mesh is then exported to a STL file which can be imported into Abaqus and Meshlab. It is noted here that the conch mesh, which is generated with a periodic function, has smoother surfaces than the spinodal meshes, which seem to have some surface roughness caused by the numerical solution to the Cahn-Hilliard equation.

2.2.2 Mesh Cleaning

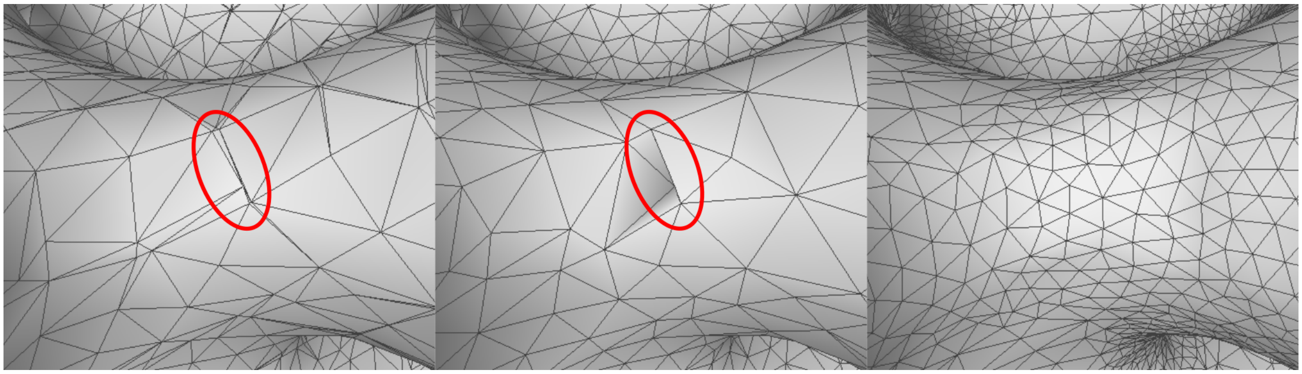

Figure 2.3: The process of mesh cleaning with a bad mesh on the left, showing numerous high aspect ratio elements. After a round of automated mesh cleaning, most of the high aspect ratio elements have been eliminated, but one in the red circle in the middle image remains. This was corrected and the mesh refined in the right image.

The isosurface function creates many elements with a high aspect ratio, so mesh cleaning is required, as shown in Figure 2.3. High aspect ratio elements can cause slow FEA simulations because the Abaqus/Explicit time step is proportional to element area, which tends to be low for high aspect ratio elements. A script was developed in Meshlab to automatically complete much of the cleanup; the process is shown in Figure 2.4. First, isolated faces were removed, in which the total number of elements are small compared to the size of the mesh. Although the spinodal structure should be bicontinuous, around the edges of the structure, there may be isolated components separated from the main structure. Non-manifold edges

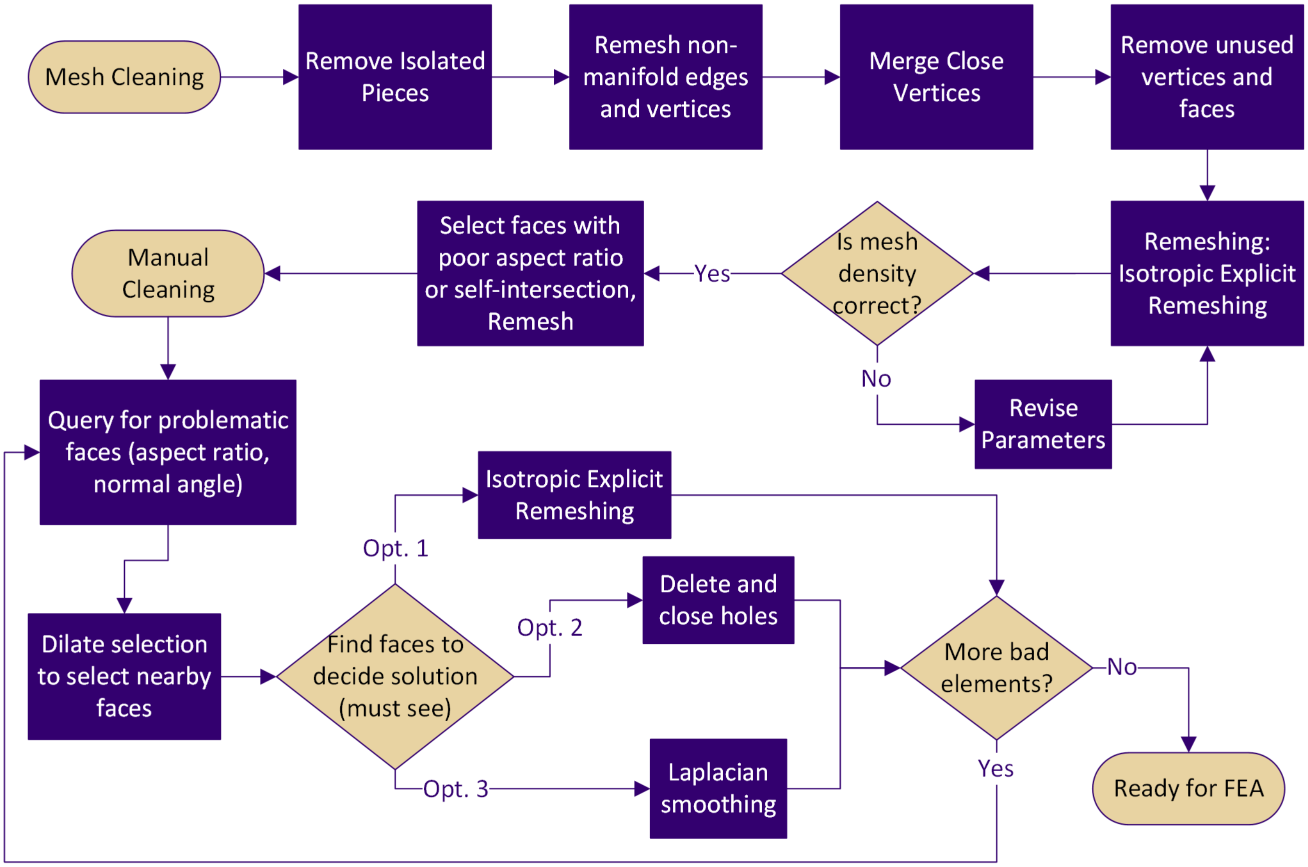

Figure 2.4: Flowchart of automated and manual mesh cleaning, to remove mesh features which may cause FEA errors.

(edges sharing more than 2 elements) and vertices (where two surfaces connect at a point) are removed and the holes patched. Close vertices are merged, in order to remove elements with high aspect ratio. This may result in some non-manifold edges and vertices so it is necessary to check again for them. Duplicate elements and vertices are merged, and zero area faces are removed. The "Isotropic Explicit Remeshing" filter is used to produce a mesh with a consistent aspect ratio. This is operated on the entire mesh, and multiple attempts may be required to reach a desired mesh density. Additional checks for faces with excessive edge length, poor aspect ratio, excessive normal angle, or which are self-intersecting are done, and these faces are selected and locally remeshed.

Even after the automated script, some manual cleanup is required, which involves searching for elements which did not get detected or properly cleaned by the standard script. This may require visual inspection of an area of the mesh to determine the best solution, since simpler issues could have already been resolved through the automated process. A query is done to find self-intersecting elements, elements with high aspect ratio, or elements with high angles to adjacent elements. Based on the visual inspection, three options to correct issues were used: Isotropic Explicit Remeshing, deleting the erroneous area and closing the hole, or using Laplacian smoothing. Based on the experience of doing this mesh cleanup, Laplacian smoothing is generally the best choice. The Laplacian smoothing filter in Meshlab was found after much of the mesh cleaning was already done, and for future mesh cleaning operations, it would be useful to add to the automated script. After cleanup is completed, the STL file is imported into Abaqus to run simulations.

Figure 2.2: A 2D slice of the GRF for the gradient architecture. The red curves represent the position of the isosurface in the structure.

2.2.3 Mesh Refinement

In order to support the requirements for mesh convergence (see Section 3.4), a process for mesh refinement is required to allow the use of smaller elements than were originally in the mesh. It is trivial to remesh the entire mesh, but finding and remeshing the critical faces was done using these steps:

- Faces with greater than 10 degrees of angle between them are selected.
- Faces with vertices along the outer surface of the model are removed from this selection.

- The selection is dilated and eroded to eliminate small isolated selections from the overall selection.
- “Isotropic Explicit Remeshing” filter is used on the selection to produce a finer mesh in areas with higher curvature.
- The mesh refinement may result in additional mesh errors, which must be manually cleaned.

Chapter 3

FEA MODEL AND STUDIES

3.1 Finite Element Model Setup

The large strain applied to the structures results in very large deformations and rotations which change the problem as a function of time. To best capture the time dependence of the problem, Abaqus/Explicit was used, with the S3RS element type. Abaqus/Explicit calculates the structural state with an iterative process at many time steps, so effects such as buckling and post-buckling behavior are captured, which cause issues for standard FEA algorithms.

The FEA model setup for this study was developed to represent the experiment described in Section 1.7. Each of the 5 architectures was tested with shell thicknesses of 5nm, 10nm, 20nm, and 40nm. While the experiments did include tests on 80nm thick shells, their behavior was primarily fracture dominated and was outside the scope and predictive power of this model.

The material model used was taken to be fully elastic with no plasticity or damage, amorphous alumina (Al_2O_3) with properties of E=164GPa, ν=0.24[42]. Material density is ρ=3.85g/cm^3, which is comparable to the wide range of accepted values[43]. Yield and ultimate strength are not included in the material model. While the architectures studied here have shown fracture damage in previous experiments, this model was developed to study buckling as a localization mechanism in the architectures, and to show regions of high stress. Fracture data for amorphous alumina is unavailable and would be too computationally intensive to provide a reasonable amount of data.

Each model was tested to 12.5% strain to observe the elastic response, plateau stress, and recovery. The 10nm models were additionally run to 30% and 50% strain. This was done because the 10nm architectures experience much less damage than the 40nm architectures, which noticeably start cracking after 10% strain.

The nanoindenter was represented with an analytical rigid mesh which was translated with an average strain rate of 0.01, using smooth step displacement, and fixed in translation and rotation. The spinodal mesh allows all degrees of freedom at the interface to the nanoindenter. The bottom of the spinodal mesh is fixed in translation, but rotation is allowed. The entire model has general contact applied to prevent interference between surfaces.

3.2 Mesh Type

The isosurface function in MATLAB produces a mesh of 3 node triangular elements, providing a choice of S3R and S3RS element types. The S3R element is a general use shell element designed to work with standard and explicit simulations[44]. It is intended to eliminate shear locking by using an assumed strain distribution and uses a single integration point[45]. This element is applicable to problems with large membrane strains, as the thickness of each element is updated as each element is strained[44]. The S3RS element is designed to be used when element membrane strain is small, because the change in thickness of the shell is not accounted for in the formulation. The excessive stiffness observed by triangle elements is dealt with by introducing a shear flexibility factor which can reduce the transverse shear and increase flexibility of the mesh. It works only in Abaqus/Explicit due to the formulation using strain rate $\hat{\epsilon}$, also referred to as velocity strain[46]

$$\hat{\epsilon} = B\hat{v} \tag{3.1}$$

where B represents the FEA B matrix, and $\hat{v}$ represents the nodal velocities in the local coordinate system. Because the S3RS element is specifically designed for use in Abaqus/Explicit simulations, it is used for the simulations shown in this work.

The difference in yield stress between the mesh types was variable in the spinodal meshes. Running simplified tests to compare results showed no differences between the results of the two meshes, but the spinodal meshes are significantly more complex and difficult to pinpoint the cause of any differences. The main disadvantage to the S3RS is inaccuracy that may occur due to large membrane strains, but few elements were observed with very high membrane strain, but few elements were observed with such high membrane strain, so any error is likely to be small.

3.3 Indenter and Test Sample Imperfections

In our samples, the bottom of the sample is fixed to the substrate, but the indenter may not be perfectly flat, and this is represented by using an analytical rigid top plate with a curvature so that the sample is gradually contacted by the indenter. This has little impact on the plateau stress, but it creates a toe region similar to the experimental data. In some experiments, the entire sample is warped and not firmly adhered to the substrate, peeling upward at the edges; the indenter is observed to not make immediate contact with the entire surface of the sample[15].

3.4 Mesh Convergence

An ideal mesh density produces accurate FEA solutions while limiting computation time, with a finer mesh producing more accurate results. The conch architecture was used to study mesh convergence, and showed significant sensitivity to mesh density, shown in Figure 3.1. To address this problem, selective mesh refinement was used to allow mesh convergence with fewer elements. The changing plateau stress is related to the onset of shell buckling, so remeshing targeted places where buckling onset would be sensitive to mesh density. A coarse mesh will not allow the formation of localization bands that are critical to determining the overall performance[47]. Areas of high curvature (high element-to-element angle) were refined, and this resulted in a stress-strain curve similar to the fine mesh. Further refinement of the curved areas led to convergence of the results with 1.98 million nodes.

Mesh density was studied using a cylinder of similar size to the test structures described in Appendix B. The point of convergence in the conch was consistent with the mesh seed

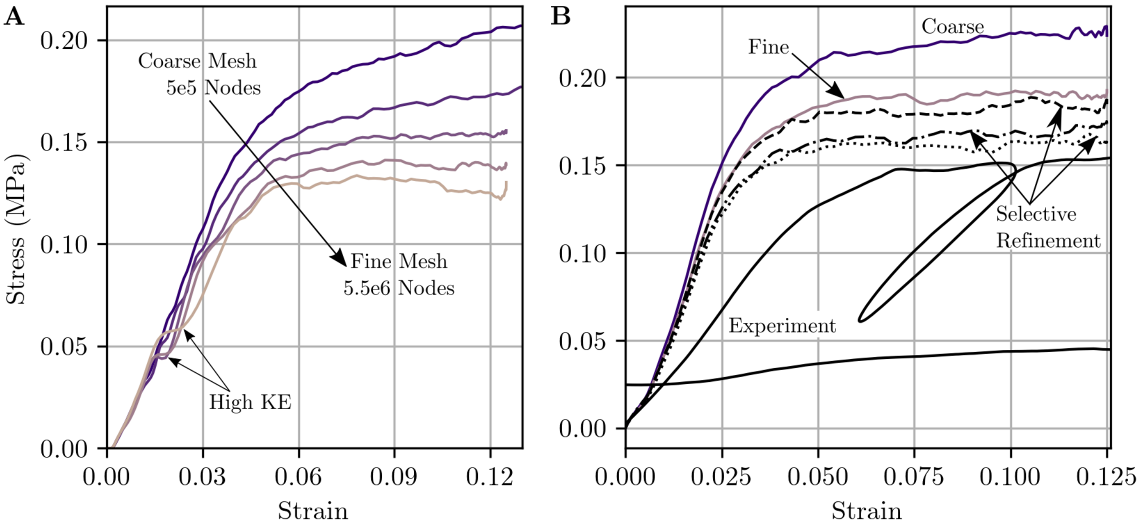

Figure 3.1: (A) Mesh size dependence of the conch architecture, showing lack of convergence up to 5.5 million nodes. These tests show evidence of high kinetic energy due to high mass scaling required to complete these simulations. No further tests were done with a finer mesh, since computing time was excessive. (B) Impact of selective mesh refinement of the conch mesh. The coarse and fine meshes have homogeneous mesh density. The 3 curves described as "Selective Refinement" (dotted and dashed) are 1.27, 1.98, and 2.4 million nodes, from top to bottom. The 2.4 and 1.98 million node meshes are sufficiently close together to indicate convergence at the lower level.

size in the cylinder tests, so the same parameters were used for each mesh. The process described in Section 2.2.3 was developed to support this mesh convergence study with the final mesh refinement step targeting an element edge length of 0.0004mm. The outside flat surfaces and the internal areas with low curvature (minimal element-to-element angle) were also refined, but neither of these attempts resulted in a different result from the comparable unrefined mesh, and are not shown in Figure 3.1B.

3.5 Mass Scaling

Mass scaling artificially increases the mass of elements to increase the time increment for each iteration of the simulation. This increase in mass can result in high kinetic energy which can affect the results of quasi-static simulations. The minimum time step of the S3RS element is proportional to the area of the element and the square root of the density, so larger elements and higher density elements will decrease computation time[46].

Each of the architectures was simulated with three steps to allow for different mass scaling target time increments, where a larger increment indicates a faster solution. The first step was given a time step of 0.03ms during the initial stiff elastic response. The second step increased the mass scaling time increment to 0.05ms due to a softer response after the onset of buckling. The third step used a smaller time increment of 0.02ms as larger increments caused errors.

To determine mass scaling parameters, tests were run with a variety of target time increments to ensure that the ratio of internal energy to kinetic energy is low, and that the load-displacement curve does not show evidence of high kinetic energy, such as shown in Figure 3.1A. A model-wide mass scaling factor resulted in excessive kinetic energy and simulation time, a target time increment was used, scaling each element until the desired time increment is reached. Using these target time increments kept the ratio of internal to kinetic energy high for each of the simulations described in this work.

3.6 Parameters not Included in Final Model

In addition to the FEA parameters used in the final models, a number of additional parameters were studied and found to have little effect on the results, especially localization. Other parameters were deemed too complex to include in this study and could be included in future versions of this work.

3.6.1 Model Distortion and Preload

The test samples have some reduction in size from the original printed size, typically on the order of 10 to 15% in height and width at the free top surface. The bottom surface is adhered to the substrate and does not see a change in size, so the structure tapers from the original width to the reduced width in the lower third of the structure. This distortion was introduced into the model to investigate if it caused any change to the results, but the reaction force remained unchanged, and no localization was induced.

The distortion was introduced by changing the node locations in the Abaqus input file and did not add any residual stress. Because the model has shrunk at the free surfaces but remained attached to the substrate at the fixed surface, it may be assumed that some residual stress exists in the model in the area close to the substrate. In order to determine this preload, the model size was reduced to the as-tested size, then stretched at the substrate to return them to the undeformed position. This resulted in a tapered structure similar to that observed in the experiments. Following this deformation, the structure was compressed in the FEA simulation. This did not result in an increased chance of localization compared to the undeformed model, and preventing model errors required displacement to be kept unrealistically small.

3.6.2 Model Damage and Waviness

Attempts were made to introduce sinusoidal waves into the mesh in order to represent the imperfections of the experimental model, seen in Figure 3.2. Waviness may come from the layer by layer building of the structure, reflection off the silicon substrate causing errors in writing, or vibration during printing.

It was hypothesized that the waviness of the experimental samples would have the effect of reducing the stiffness of models by promoting the onset of buckling throughout the model. In addition, if the waviness was found only at the bottom, this could explain the localized collapse of the 10nm experimental samples.

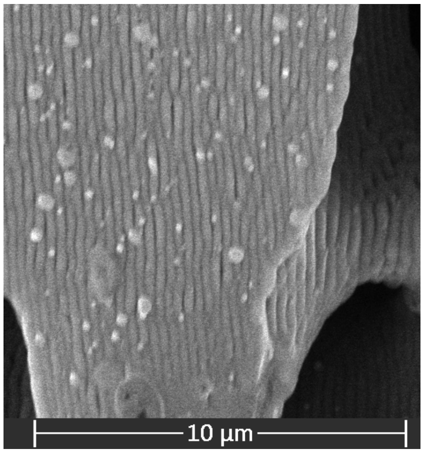

Figure 3.2: Waviness observed in the experimental sample.

Full model waviness did have the effect of reducing the initial model stiffness as well as the plateau stiffness. While this was desirable for matching experimental results, the wavelength and amplitude required to achieve these results were not representative of the imperfections in the experimental samples, requiring very large amplitude (0.3μm) and wavelength (5μm). The short wavelength of the experimental samples (relative to the mesh size) resulted in poorly formed elements which required extensive model cleanup to address.

Waviness in the bottom layer was modeled as sinusoidal waves decreasing in amplitude up to 25μm above the substrate. This also did not result in localized deformation of the bottom layer in the simulation, indicating that the sample waviness was not a factor in this localization.

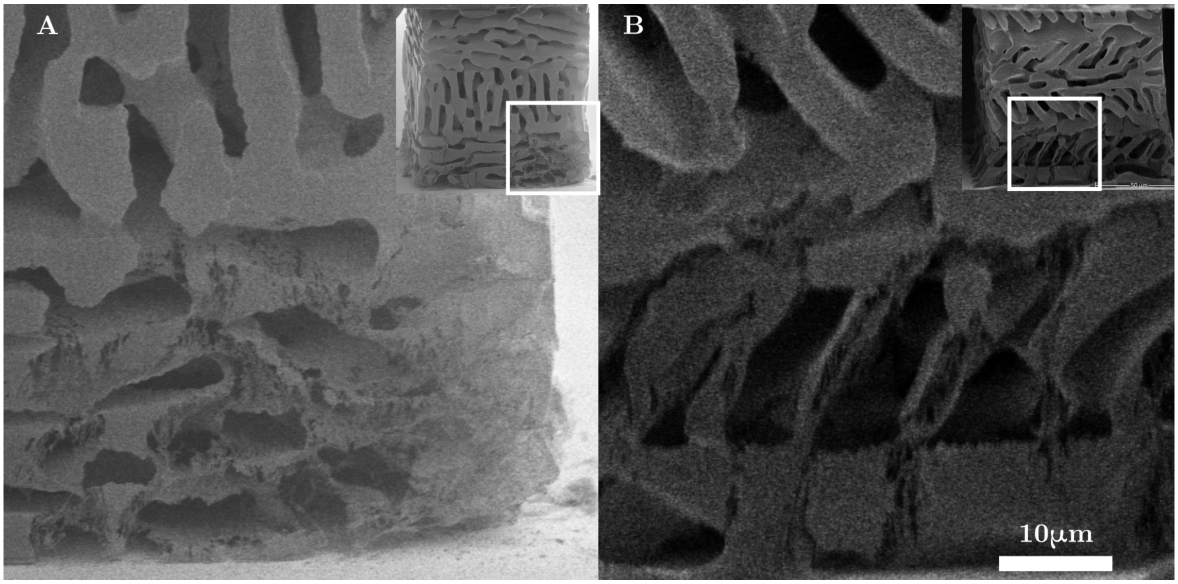

Figure 3.3: 10nm conch and gradient experimental samples, showing substantial FIB-induced damage on the sides of the structures, in areas which exhibited localized damage.

The FIB is intended to damage the non-critical top surface of the structures, but the side surfaces were also damaged in some of the 10nm structures, as seen in Figure 3.3. This damage was not duplicated in the final FEA model, though it may have had some impact, and this is an area of future work.

3.6.3 Changes to Top and Bottom Boundary Conditions

Boundary conditions changes were tested at both the top and bottom interfaces. Tests were done to allow additional degrees of freedom in the top interface, including rotation and translation of the indenter, which resulted in additional model instability but no change in stiffness or localization. The bottom surface was similarly revised to constrain only z displacement with no change in results. Other simulations were run with the bottom surface elements removed completely. It is assumed that in the tested samples, the bottom surface would be absent due to adhesion between the build scaffold and the substrate. With this bottom surface removed, and a variety of boundary conditions tested, there was no change to the mechanical properties or strain localization of the model.

Chapter 4

RESULTS AND DISCUSSION

4.1 Results

4.1.1 Experimental Results and Correlation with FEA Results

The experimental data summarized in Table 4.1 shows the difference in performance between different architectures and the 10nm and 40nm shell thicknesses. The 10nm samples each show localized buckling deformation at the bottom of the structure, with no visible fracture damage. By the time the full 0.5 strain is reached, the entire structures have buckled or otherwise deformed, but each structure fully recovered. In the columnar architecture, the buckling is particularly pronounced, while in the conch architecture, some layers do not show full collapse. The 40nm samples show fracture damage close to the indenter, but the post-yield behavior varies by architecture, with none of the samples showing evidence of elastic buckling. The columnar and iso samples continue to localize fracture at the top, with

Table 4.1: Experimental results, in terms of localization, damage, and recovery.

Arch.	Thickness	Localization	Visible Damage	Recovery
Col	10nm	Bottom; Shear Band	None	Full
Col	40nm	Top; Shear Band	High	91%
Conch	10nm	Bottom	None	Full
Conch	40nm	Minimal	Some layer collapse	Full
Grad	10nm	Bottom	None	Full
Grad	40nm	Bottom, then top	High, in lamellar layers	98%
Iso	10nm	Bottom	None	Full
Iso	40nm	Top, Shear Band	High at top and in shear band	90%
Lam	10nm	Bottom	None	Full
Lam	40nm	Bottom	Some layer collapse	N/A

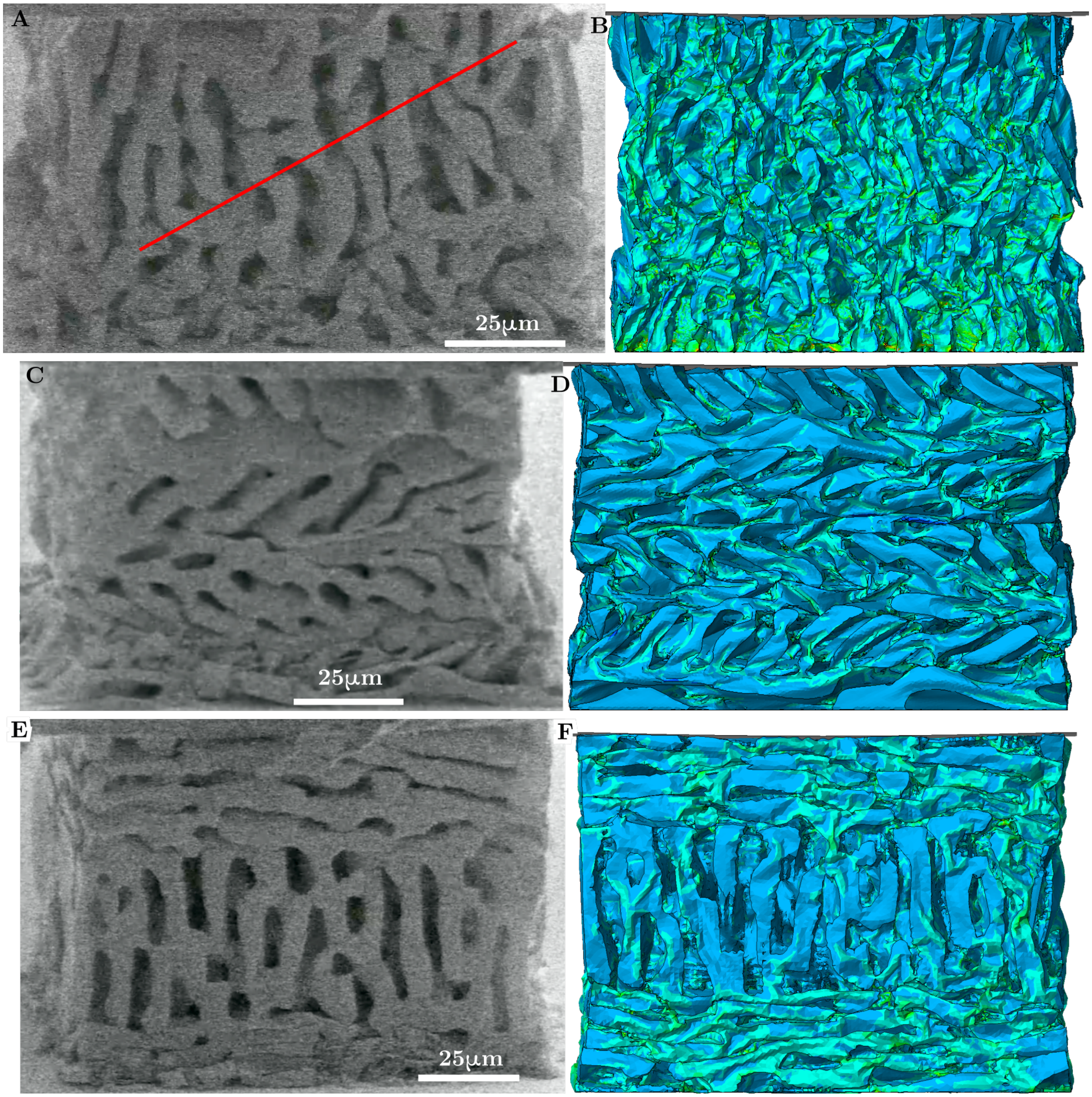

Figure 4.1: Comparison of experiments and FEA simulations of 10nm columnar, conch, and gradient architectures at 0.3 strain. The columnar experiment (A) shows localized collapse at the bottom near the substrate, as well as a shear band following the red line. The FEA (B) shows substantial buckling of the columns, but not in any aligned way that could be considered a shear band. (C) The conch experiment shows localized collapse at the bottom near the substrate, while the FEA simulation (D) shows more localized deformation in the center of the structure. The gradient architecture experiments (E) and FEA (F) both show the lamellar portions at the top and bottom having collapsed, with columnar section in the middle largely unaffected. The experiments show that the bottom layer has collapsed more than the top, while the FEA results show no such localization.

additional fracture bands forming at high strains. The conch shows delocalized deformation; some fracture bands form at high strain, but these do not spread between layers. Only the conch architecture fully recovered at 40nm. The gradient and lamellar architectures do not show much fracture until 0.25 strain, but the gradient architecture, having the stiffer columnar band, shows significant damage to the lamellar bands at high strains but still shows good recovery. 80nm samples were also tested, but the results were largely dominated by fracture, so no FEA simulations were conducted at this thickness.

Figure 4.1 shows a comparison of selected FEA simulations with experiments at 10nm shell thickness and 0.3 strain. The columnar structure shows localized deformation at the bottom in the experiment, and also the formation of a shear band. The FEA simulation of this model shows substantial buckling of the columns, but a shear band is hard to discern clearly. The conch experiment shows substantial localized deformation at the bottom, with little change at the top. The FEA simulation shows localized shear deformation in the middle of the structure, but not the collapse at the bottom. The gradient structure shows the lamellar sections collapsing, while the columnar section has not begun to deform, with the experiment showing more deformation in the bottom lamellar band than the top.

4.1.2 Stress-Strain Curves and FEA Model Validation

The FEA data was validated against the experimental data using the stress-strain curves shown in Figures 4.2 and 4.3. Stress and strain for the whole structure were calculated from the load and displacement outputs from the nanoindenter and FEA simulation, and using the nominal size of the model of 0.125mm on each side, to provide a consistent calculation despite the reduction in size of the experimental samples.

Reproduction of the experimental behavior was focused on matching the initial linear elastic response and the initial yield stress. Based on the results of the 40nm tests, which show values of elastic modulus and yield stress close to the experimental values, it appears that the FEA model produces results consistent with the experiments.

Each of the FEA stress-strain curves shows a similar path, in which there is an initial

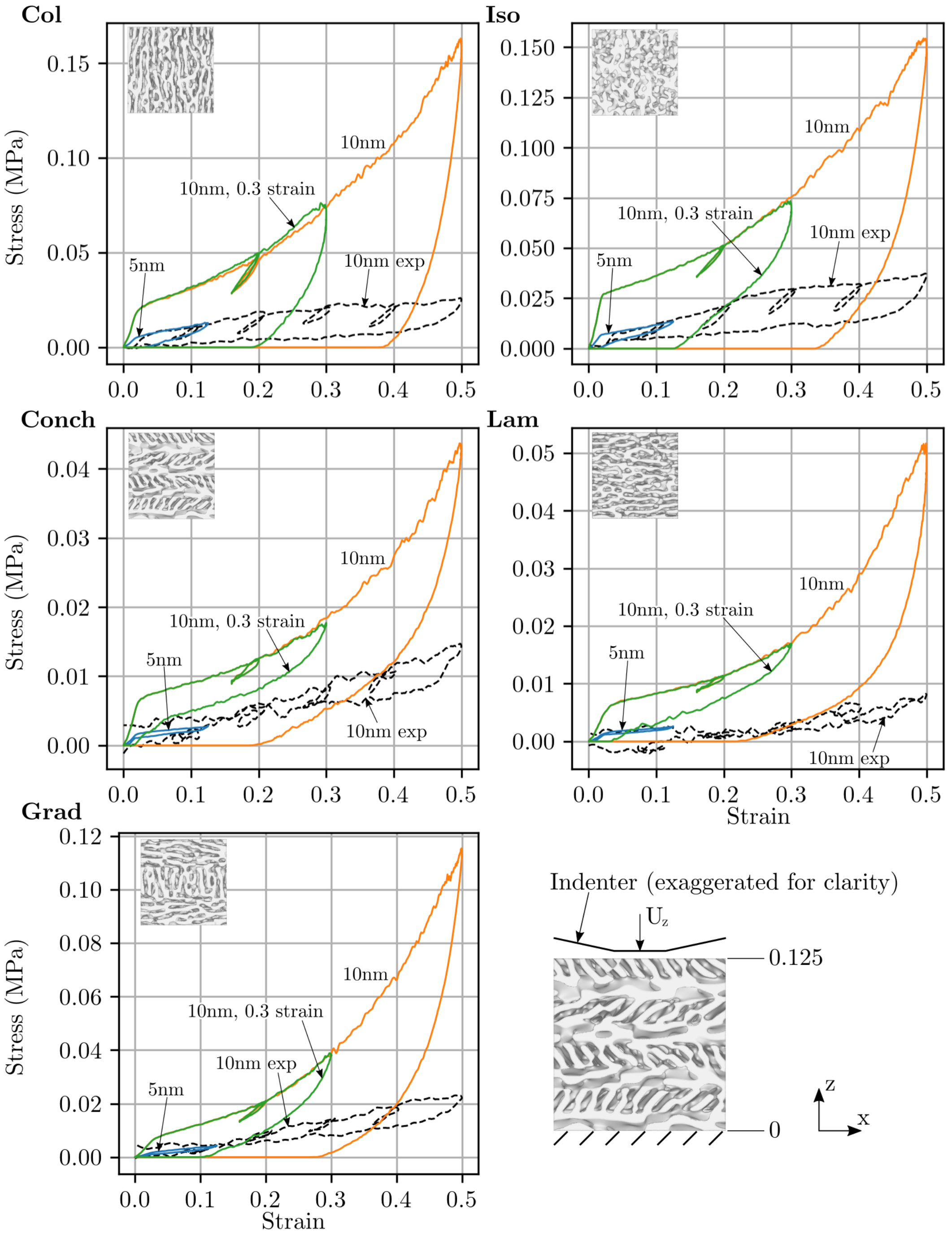

Figure 4.2: Stress-strain curves for the 5nm and 10nm simulations and 10nm experimental data. When comparing the FEA simulations to the experimental data, the 5nm FEA matches best with the 10nm experiments. The results for the Conch, Lamellar, and Gradient experiments show such low stress that an initial elastic response cannot be calculated, due to the high level of signal noise.

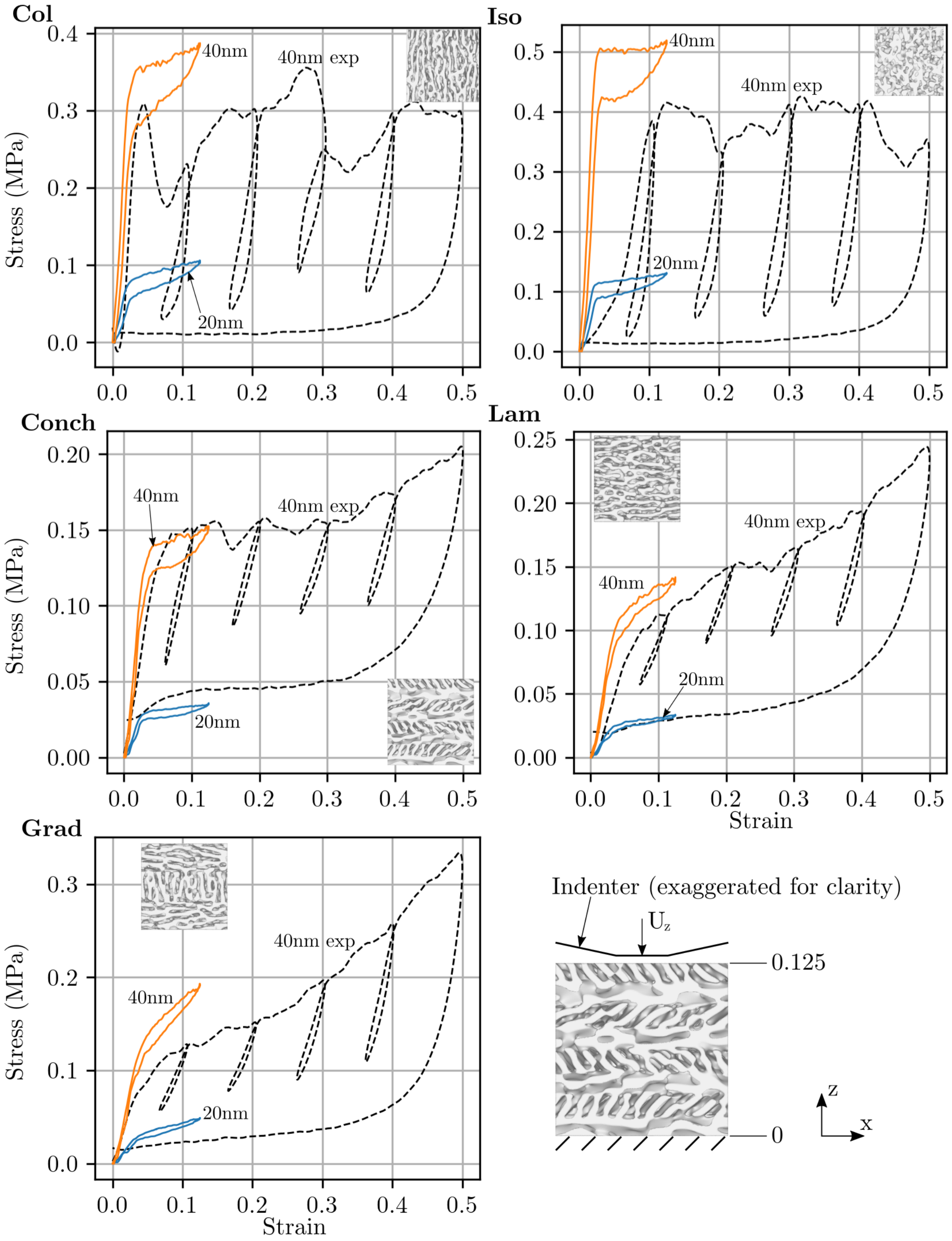

Figure 4.3: Stress-strain curves for the 20nm and 40nm simulations and 40nm experimental data. The 40nm FEA matches well with the corresponding experiments.

linear elastic response, which eventually levels off at a plateau stress. This plateau stress is used as a yield stress point, but it is caused by buckling, not plastic deformation. The 10nm experiments show results that align closely with the 5nm FEA simulations. This result may be due to underestimation of the coating thickness during ALD. The conch, lamellar, and gradient samples at 10nm each are so soft that there is no clear elastic response due to the high amount of noise in the load output. The 10nm simulations show that the stiffness at this plateau point increases with strain, due to increasing contact between layers of the shell increasing the critical buckling load, and leading to a stiffer response.

The impact of fracture on the results of the experiments is substantial in the 40nm tests. In the columnar, conch, and isotropic samples, fracture occured primarily near the indenter, however the columnar and isotropic samples continued to fracture as the test progressed, resulting in repeated softening shown in the stress-strain curve. The conch, gradient, and lamellar structures showed much less fracture, and as a result, some post-yield hardening is seen, similar to the experimental results. Although the 40nm simulations were not taken to the full 0.5 strain, the 10nm samples show significant hardening after yield, similar to the results for the 40nm lamellar and gradient experiments which exhibit less fracture than other samples. From this, it appears that the columnar and isotropic spinodal architectures are more prone to fracture than the softer conch, gradient, and lamellar architectures, which show post-yield hardening similar to the FEA simulations.

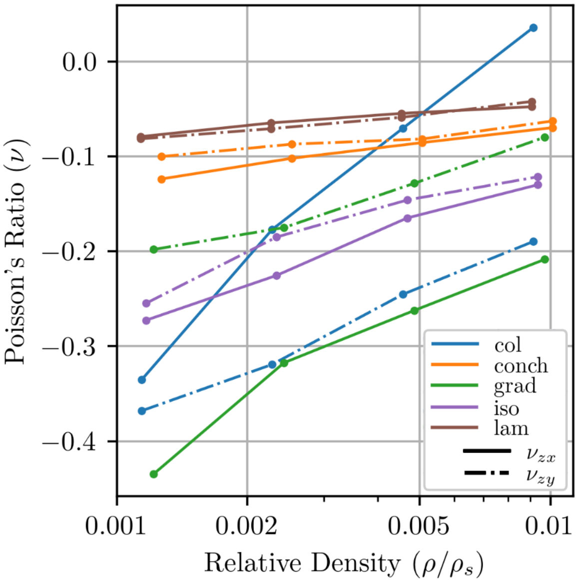

Figure 4.4: Poisson's Ratio (ν) is calculated from the average strain values in x, y, and z directions. Auxetic behavior decreases (less negative ν) as the shell thickness increases.

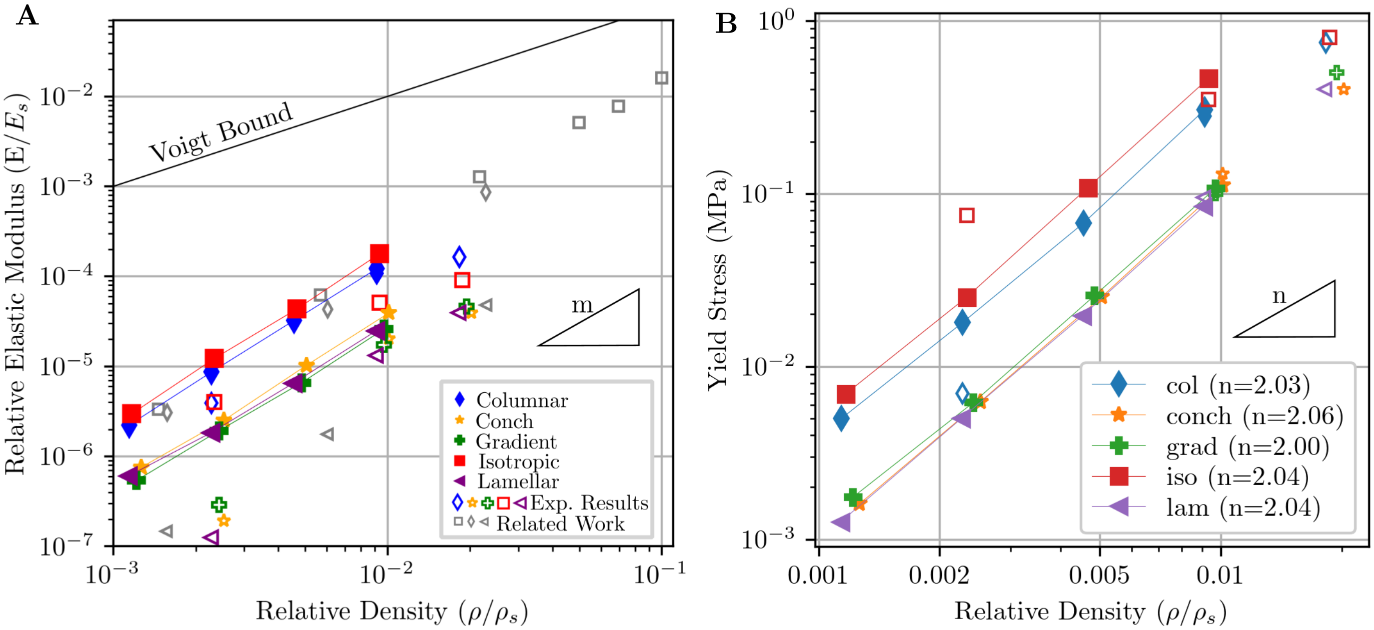

Figure 4.5: (A) Scaling of elastic modulus from this work compared to similar works[15, 20], showing consistency with the scaling trends of prior works and the experimental results. Scaling exponents: m = 1.92 (col), 1.91 (conch), 1.89 (grad), 1.99 (iso), 1.82 (lam). (B) Comparison of yield stress values from this work with the experimental results. The yield stress of experiments and simulations at $\bar{\rho} = 0.1$ (40nm) are close, but at 10nm shell thickness the isotropic performed better than simulations, and the columnar performing worse; other architectures did not demonstrate a yield stress.

4.1.3 Material Properties

The basic material properties from each simulation were calculated from the stress-strain curves and the strain field described in Appendix C. The elastic modulus was calculated based on the highest slope of the stress-strain curve prior to yield. Yield stress was calculated at a 0.2% strain offset. Most notably, every simulation showed auxetic behavior of the architecture, shown in Figure 4.4, and this auxetic behavior decreases with shell thickness, with the only the columnar 40nm simulation showing a positive ν_{zx}. As the material thickness increases, so does the buckling critical load, so the change in poisson's ratio likely relates to buckling properties of the architectures. Poisson's ratio is also not constant through the simulation, although it is uncertain if this is a material effect, or the result of the the sampling of displacement outputs.

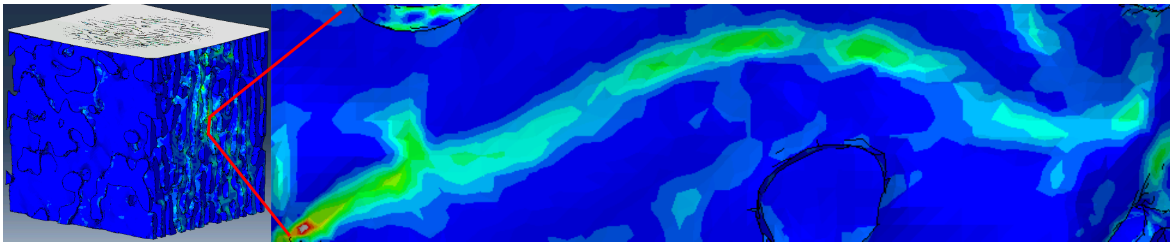

Figure 4.6: A band of stress caused by buckling in a vertical lamella prior to yield stress, likely contributing to the low stiffness of the columnar architecture.

The comparison of elastic modulus and yield stress between different architectures and with experimental data is shown in Figure 4.5. The elastic modulus for these simulations is consistent with previous works at similar relative density as well as higher relative density in a structure that experienced plasticity.

The columnar architecture consistently shows slightly lower stiffness and yield strength compared to the isotropic, despite containing more direct load paths from the indenter to the substrate. However, during the initial elastic response, the columnar architecture shows long bands of shell buckling, such as the one shown in Figure 4.6, which may lead to a reduction in stiffness, even early in the simulation prior to reaching the yield point. Buckling in the isotropic architecture does not show the same patterns due to the more consistent curvature. The gradient, conch, and lamellar architectures have similar elastic modulus and yield strength across the relative densities studied here, each being made of lamellae with compliant deformation modes. Even though the gradient architecture has a section of columnar architecture in the middle, the lamellar component deflects substantially so that the extra stiffness of the columnar portion has little impact on the overall modulus.

4.2 Discussion

4.2.1 Localization

The localization of each architecture is an important part of its properties. The experiments showed different modes of localized damage and deformation (see Table 4.1), and if all conditions in the experiment can be exactly replicated in the FEA, then the same localization

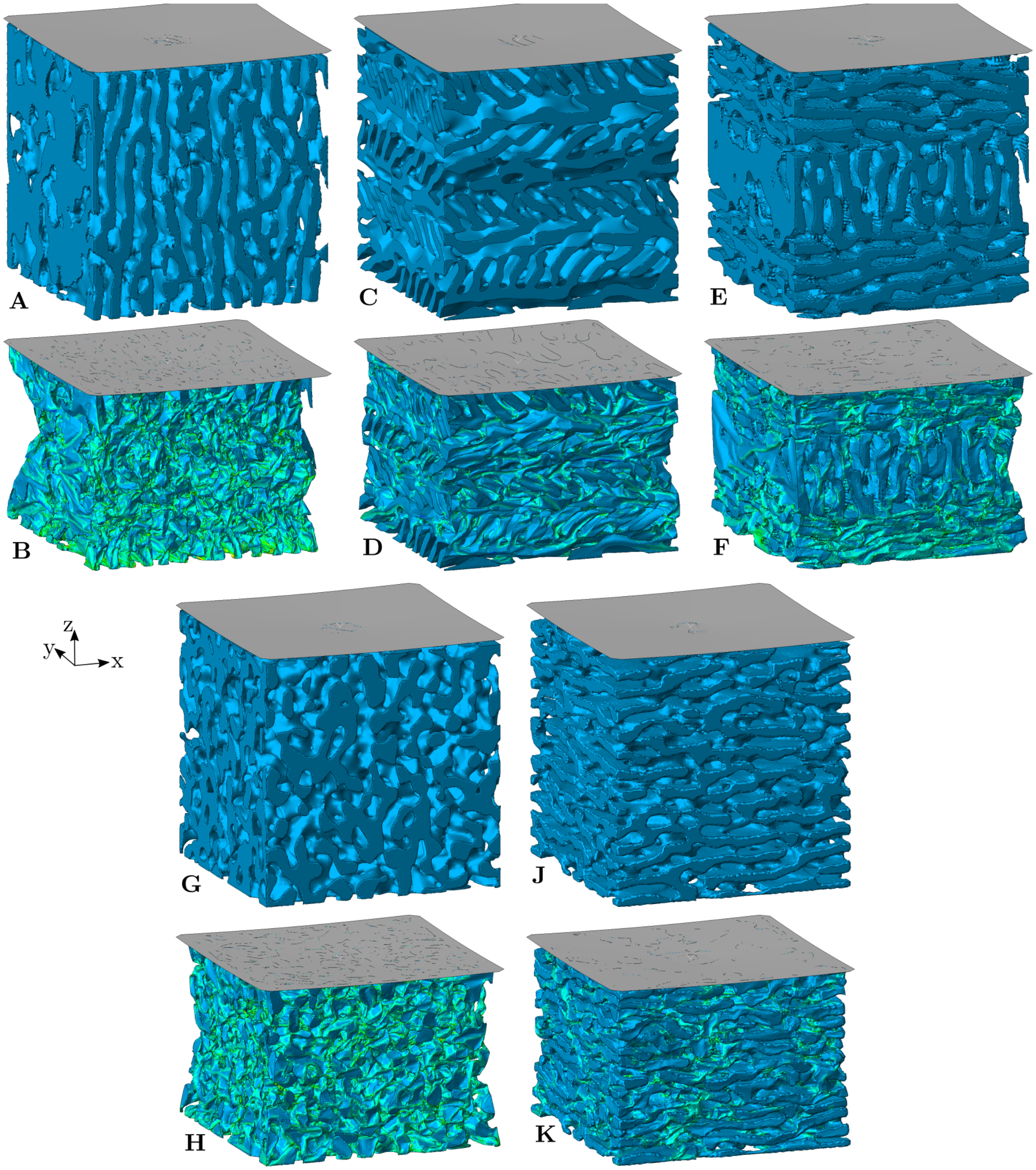

Figure 4.7: Maximum principal strain of the columnar, conch, gradient, isotropic, and lamellar architectures at 0 strain (A,C,E,G,J) and 0.3 strain (B,D,F,H,K). Auxetic behavior can be seen most clearly in B, F, and H, which are the structures with the most negative ν.

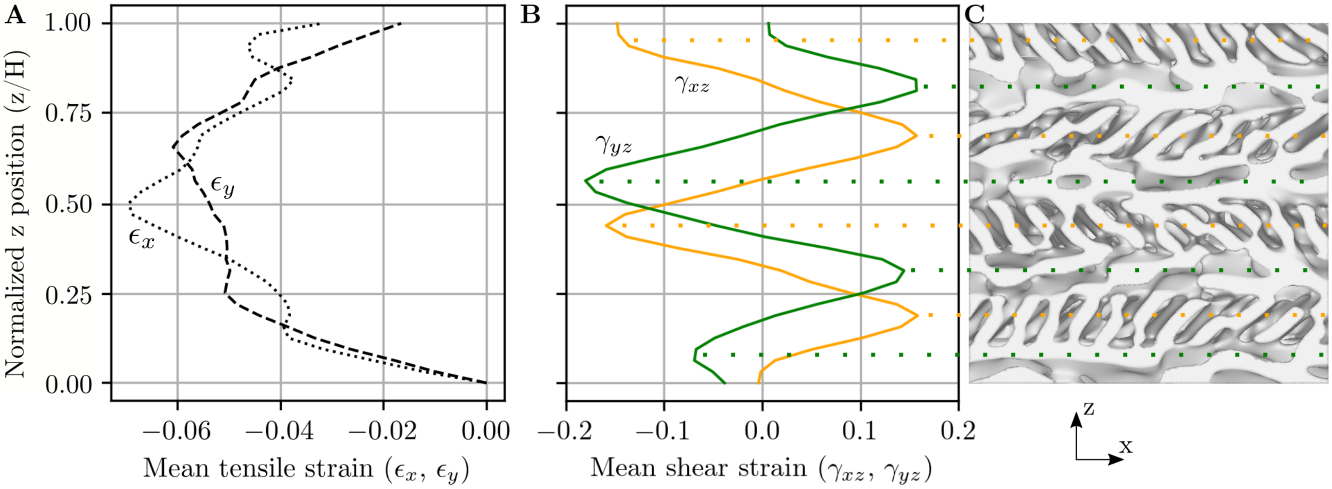

Figure 4.8: Strain in the conch architecture through the thickness at 0.3 strain. (A) Orange and Green curves are γ_{xz} and γ_{yz}. (B) Dotted and dashed curves are ϵ_x and ϵ_y. (C) Alternating directions of the conch architecture lamellae lead to alternating high and low shear strains. The peaks and valleys of the shear strain plots align with the lamella orientation favorable to such deformation.

should be seen. The FEA simulations show some strain localization, but they do not match the behavior of the experiments, which typically show localization at the top and bottom of the structures. To quantify this localization, average z strain values are calculated based on the strain field described in Appendix C. The values of the strain tensor are expected to be relatively homogeneous in x and y, but changing in z (with the substrate at z=0 and the indenter at z=0.125), so strain is averaged in x and y to show the change of strain along the z axis.

Figure 4.7 shows that the middle of the structures tend to shrink during compression, but not the top and bottom, but this is likely caused by the boundary conditions. The conch architecture exhibits shear strain localization due to the nature of its architecture, as the angled lamellae encourage shear strain in a single direction only, as shown in Figure 4.8, but this also contained shear in each layer, preventing the formation of shear bands between layers of the structure, which is consistent with the experimental results. The columnar

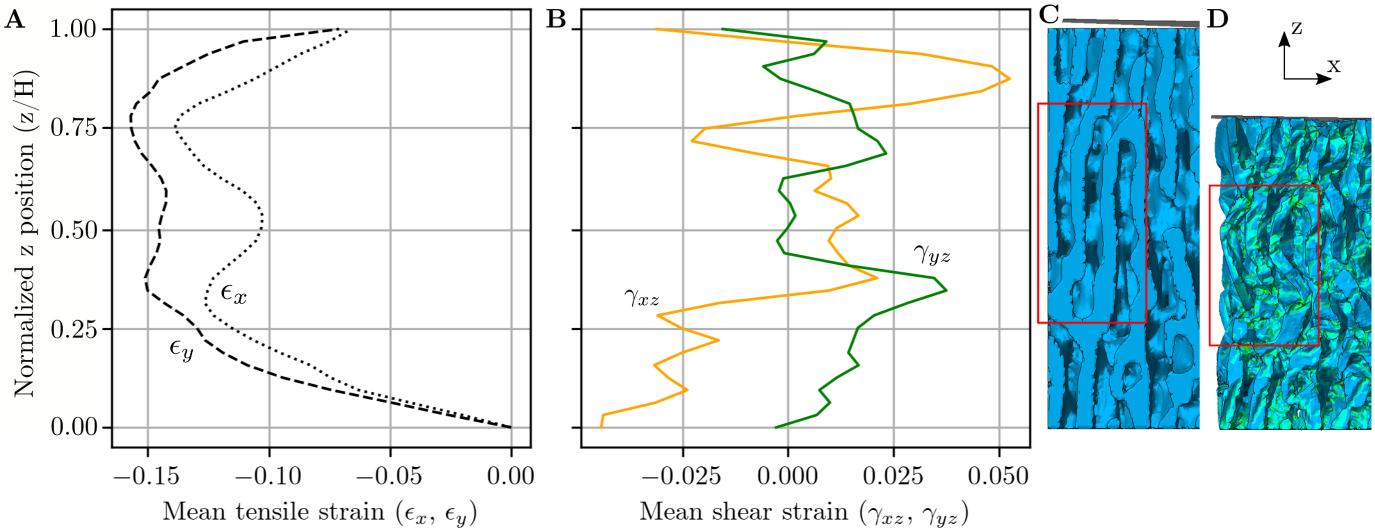

Figure 4.9: Strain in the columnar architecture through the thickness at 0.3 strain. (A) Orange and Green curves are γ_{xz} and γ_{yz}. (B) Dotted and dashed curves are ϵ_x and ϵ_y. (C) and (D) show the structure at 0 and 0.3 strain, respectively. The tensile strains are much higher than that of the conch, and different in the x and y directions, reflecting the different properties in each axis. The shear strains do not follow a pattern, but reflect some random buckling which can be seen in (C) and (D), which show substantial buckling of the columns which will be seen in the bulk material as shear strain.

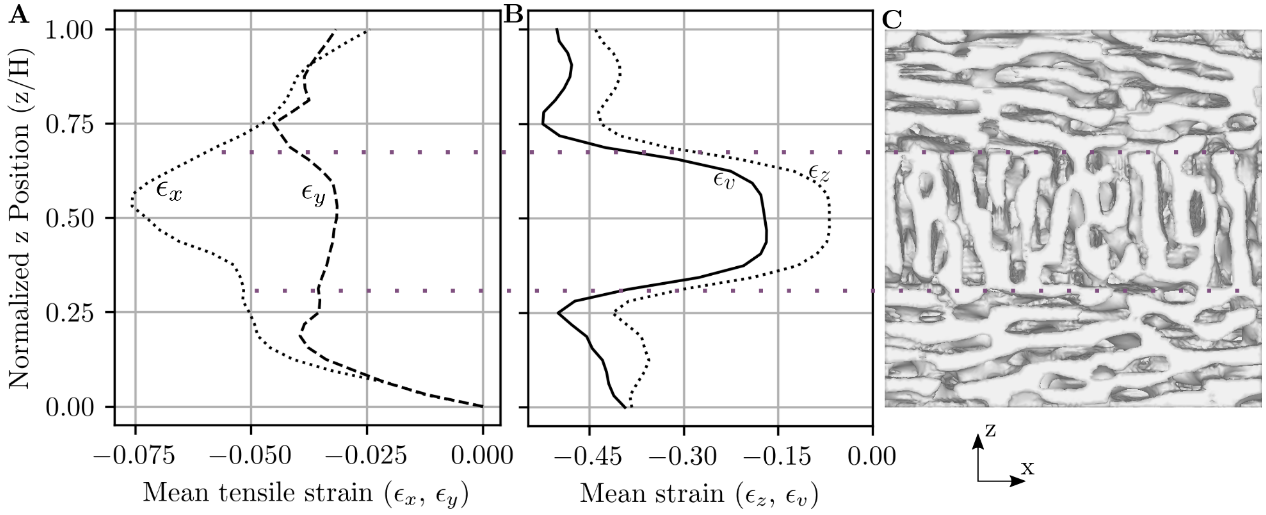

Figure 4.10: Tensile strain in the grad architecture at 0.3 strain. ϵ_z is substantially reduced in the columnar region due to increased stiffness in this region. ϵ_x is significantly higher in this area than ϵ_y due to the reduced stiffness in the x axis.

architecture, on the other hand, does not show any pattern of shear strain, as shown in Figure 4.9, but localized high levels of shear strain does occur, which may indicate some susceptibility to shear band formation, which was also seen in the experiment. The gradient architecture shown in Figure 4.10 sees a significant reduction in ϵ_z in the columnar band, due to the increased stiffness in this area. ϵ_x is also high in this area due to the higher stiffness of the y axis compared to the x axis resulting in more auxetic strain.

The localization shown in the conch (Figure 4.11) and iso (Figure 4.12) demonstrates that although the strain is not constant through the structure, the relative distribution of volumetric or shear strain does not change substantially as the simulation progresses. No

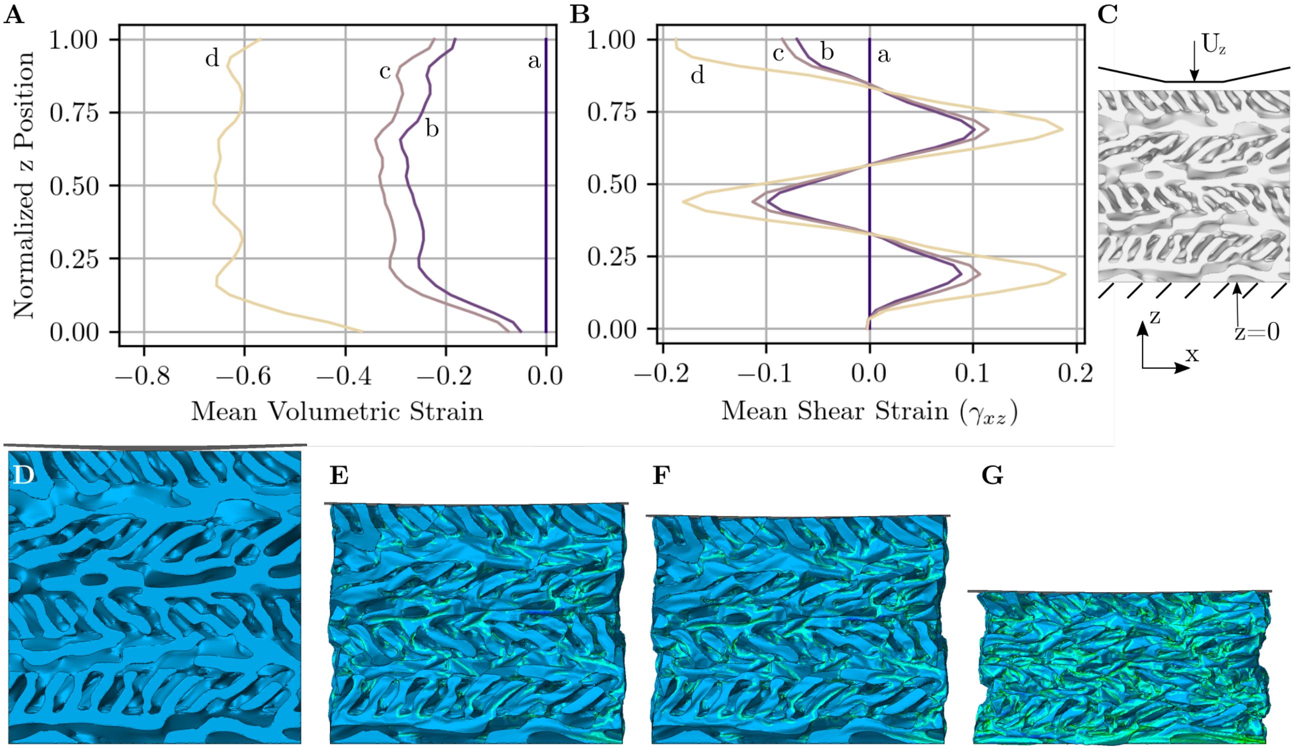

Figure 4.11: Mean volumetric (A) and shear strain (B) for the conch architecture. (C) shows the orientation and application of load. The curves marked a, b, c, d in the plots represent strains of 0, 0.2, 0.24 (after strain pullback), and 0.5, which are shown in (D) through (G), respectively. The volumetric strain is highest in the middle of the structure, reduces slightly near the indenter, and is much lower near the fixed boundary at the bottom.

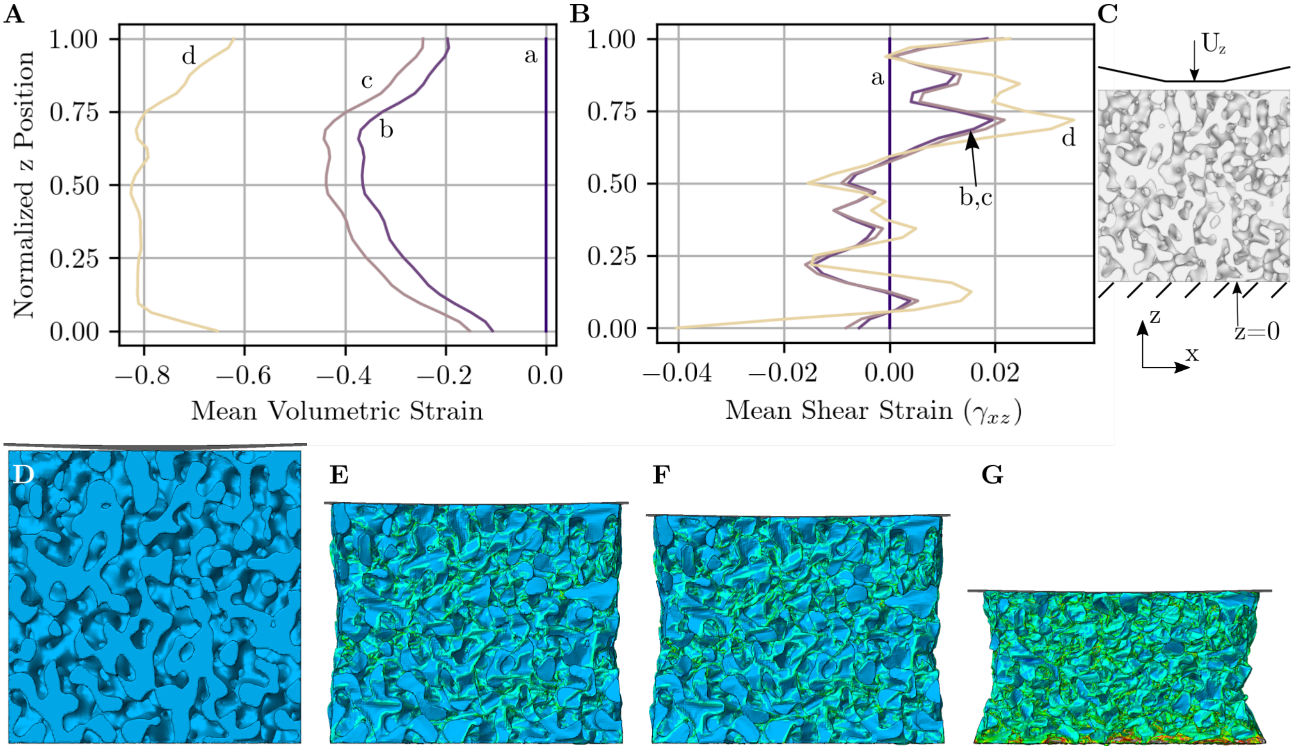

Figure 4.12: Mean volumetric (A) and shear strain (B) for the iso architecture. (C) shows the orientation and application of load. The strains marked a, b, c, d in the plots represent strains of 0, 0.2, 0.24 (after strain pullback), and 0.5, which are shown in (D) through (G), respectively. The volumetric strain is highest in the middle of the structure throughout the simulation, reflecting the auxetic behavior seen in the images. Shear strain in the iso is insignificant and more than an order of magnitude lower than the volumetric strain, indicating shear strain does not depend on vertical position.

layer collapse is observed as in lattices or the bottom layer of the spinodal shell experiments. In comparing these 2 architectures, it can be observed that the volumetric strain is significantly higher in the iso compared to the conch, due to a lesser degree of auxetic behavior in the conch, so that ϵ_x and ϵ_y are less in the conch. Only the conch shows significant shear strain, where it is about an order of magnitude higher than the shear strain in the iso, since the iso architecture does not encourage tension-shear coupling.

The experiments show localization in the form of bulk volume change, typically seen at the bottom of the 10nm structures, where fracture is not a major factor. Although some variations in volumetric strain are seen in the structures, this tends to be limited to some layers collapsing due to a stochastic lack of connectivity in a given area. The bottom layer localization is not seen in any simulation, despite many changes in simulation parameters described in Section 3.6.

4.2.2 Stress Distribution

The distribution and magnitude of strain and stress in the structure has a significant impact on the performance of an architected material. The FEA results data can provide this distribution to understand the differences between the architectures, which is shown in Figure 4.13 at 0.3 strain in each architecture. Each of the architectures show a high element count with near zero stress, and a small number that exceeds an estimated failure stress of 5GPa[48], which would have failed if damage had been included in the model. The stiffer architectures (isotropic and columnar) show higher stress, since more load is being carried, but the columnar shows higher values than the isotropic, indicating higher bending stresses, likely buckling related, which may have contributed to the low modulus of the columnar architecture. The experiment results seem to confirm this with the 40nm isotropic and columnar structures experiencing progressive fracture failure at the indenter, while the lamellar, gradient, and conch materials show moderate fracture and better recovery. The structures with a wider distribution of stress should expect to see more areas of failure from both fracture and buckling.

The stress concentrations shown in 4.13D and E suggest that buckling will occur in the architectures at a low strain, but due to the stochastic nature of the architecture, alternate load paths are available which carry loads when other members buckle or fracture. In the conch architecture, the areas of high stress are surrounded by regions with lower stress, so that any damage to occur by buckling or fracture will not affect the remainder of the structure, and can be expected to carry some load which will contribute to its full recovery.

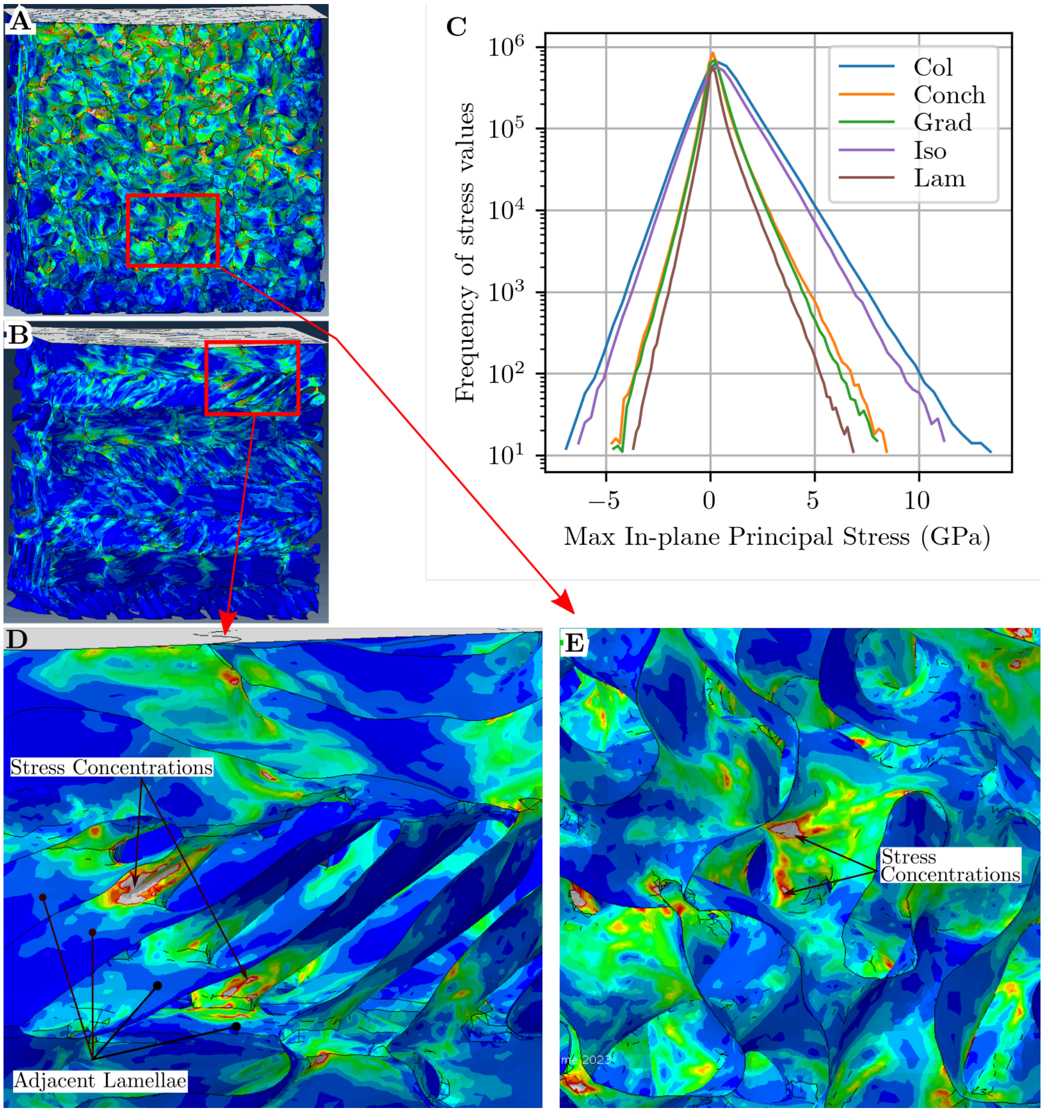

Figure 4.13: (A) and (B) show stress in the iso and conch architectures, at a midplane section cut. (E) and (D) show detail views of each of those showing stress concentrations in areas of critical connection and high curvature. This is a view at very low strain, showing high stress concentrations in a few areas. (C) Shows the distribution of max in-plane principal stress in each architecture at 0.3 strain. Probability is highest of a near-zero strain for each structure, indicating that most elements are in bending. Highest strain values occur in the stiffest structures, but the columnar shows higher strains than the isotropic indicating a cause for its poorer performance.

4.2.3 Structural Recovery

In the 0.5 strain (10nm) simulations, the structures did not fully recover to the initial state, recovering only 0.1 to 0.3 strain. The experiments showed complete recovery in the comparable 10nm tests, so some mechanism to describe this is needed.

After exceeding 0.3 strain, the viscous dissipation (ALLVD history output) and frictional dissipation (ALLFD) parameters increase dramatically causing mismatch between internal energy (ALLIE) and work (ALLWK), and a loss of stability in total energy (ETOTAL). In Abaqus/Explicit simulations, viscous dissipation is used as a mechanism to reduce instabilities in the simulation, and is governed in part by the bulk viscosity parameter defined in the model setup. It is preferred in quasi-static simulations to maintain a constant ETOTAL value, so this change indicates a lack of accuracy of further results. The 0.125 strain samples recover well and also have more stable ETOTAL value. The energy plots of the conch and iso 10nm simulations are shown in Figure 4.14.

A reduction of bulk viscosity was tested a simplifed cylinder model (Appendix B) as a method to reduce ALLVD. While some reduction occurred when reducing bulk viscosity in half, it did not result in full recoverability of the cylinder and this change caused the simulation to fail. Because viscous dissipation pressure is proportional to density, a reduction of mass scaling was tested, since ALLVD begins to increase rapidly after 0.3 strain when mass scaling was higher, but this did not substantially reduce ALLVD.

During the cylinder tests, it was observed that element viscous dissipation (ELVD field output) increased after the cylinder snapped between buckled states, and elements that experienced this may see instability which requires damping to prevent simulation failure. A comparison of two consecutive field output frames in Figure 4.15 shows a change in buckling states resulting in an increase in ELVD.

In the spinodal and spinodoid simulations, high ELVD values were primarily observed at places of self-contact, due to the effects of the general contact interaction, as shown in Figure 4.15C. At the low strain levels used for most of the tests, the level of self-contact

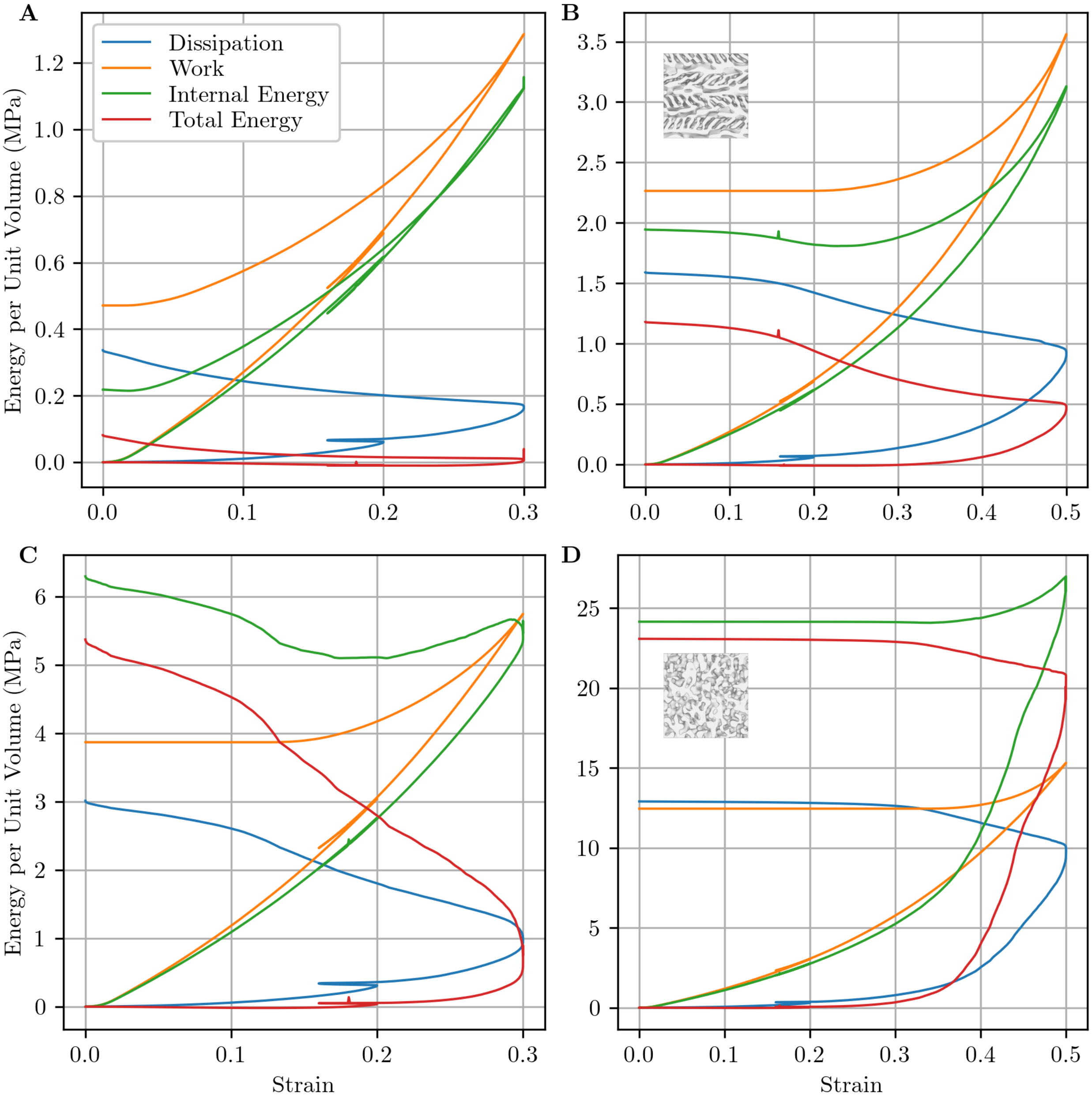

Figure 4.14: Energy balance of the 10nm conch (A) 0.3 strain and (B) 0.5 strain and iso (C) 0.3 strain and (D) 0.5 strain tests. Both the conch and iso architectures show substantial energy dissipation (frictional and viscous dissipation) in the 0.5 strain tests, but at 0.3 strain, the conch has lower dissipation, lower residual strain energy at the end of the simulation, and better recovery at the end. Energy balance of tests to 0.125 strain did not show any problems.

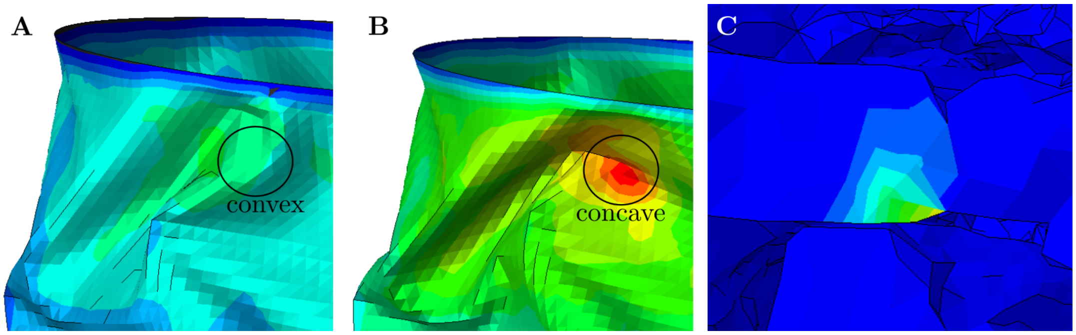

Figure 4.15: Locations where element viscous dissipation (ELVD) can be high: (A) shows the cylinder test before and (B) shows after snapping between two buckled states, causing the ELVD parameter to increase substantially. (C) shows an area of self-contact in the gradient architecture which resulted in viscous dissipation during unloading, but the contact did not release to the original state.

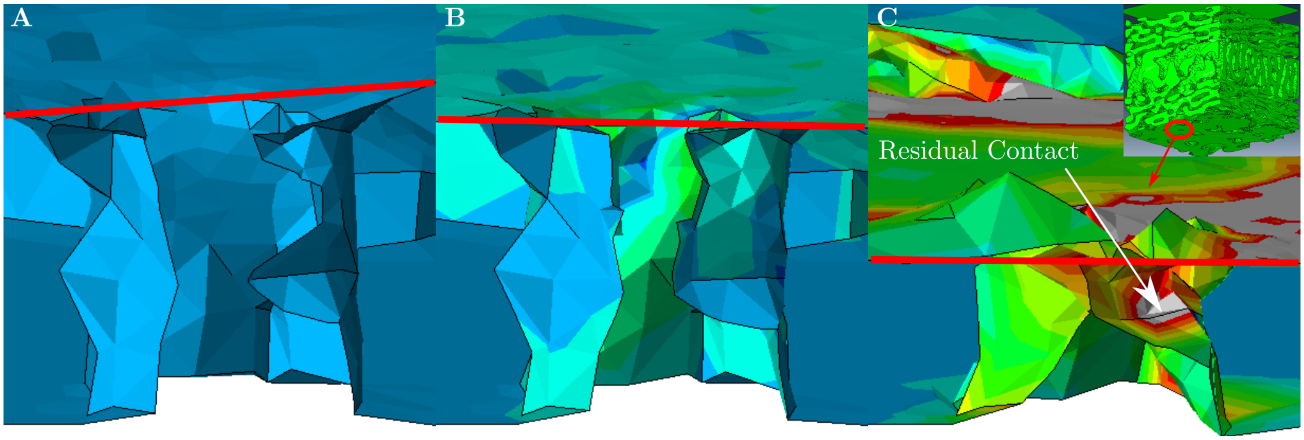

Figure 4.16: Comparison of the initial strain (A) of the gradient architecture with the final strain at the end of the test after compression to 0.3 strain (B) and 0.5 strain (C). The 0.5 strain test resulted in substantial self-contact in this feature, resulting in residual strains when the indenter returns to its original position. The 0.3 strain test shows some residual strain, but in the image there is no residual contact. Image strain scale from -0.01 to 0.04 with high positive strain represented by red or gray. The red line across each image shows the approximate location of the same lamella, showing the difference in recovery between the different simulations.

was low, so this effect was minimal. At high strain, the amount of contact is dramatically higher, and the ELVD parameter increases as well, since it appears that damping is used to prevent self-intersection of elements. The self-contact results in residual strains because the contacting surfaces do not always release during recovery, as shown in Figure 4.16. This results in a different metastable state, but one that is held in place by unnatural connections between elements. The lack of recovery in the large strain simulations likely is caused by the residual contact, but the impact of the high total energy parameter may have resulted in other undesired effects during the recovery.

4.2.4 Delocalization Efficiency

The delocalization coefficient was calculated for each architecture using Equation 1.4, with the results for 10nm and 40nm structures shown in Figure 4.17. The calculation of the strain field (see Appendix C) may have resulted in some spurious outlying values which can impact the results, so the largest and smallest 20 values were excluded from this calculation.

Each of the plots show a rapid drop from the start to the first data point, which results from the curved indenter applying strain to a localized area. After this, the linear elastic region of the 40nm shows a plateau around a value of 0.9, before dropping to a new plateau after yield. The linear elastic plateau is shown in the 5nm and 20nm results as well, but the lower frequency of data outputs in the 10nm simulations did not capture this.

The relative lack of connectivity of the shell structures is similar between the various architectures, leading to little difference between them in localization. This is particularly notable during the linear elastic response, due to minimal buckling at this stage, and with the same model setup. The gradient architecture shows larger variation in volumetric strain and an increase in localization due to the different orientations of lamellae resulting in large differences in ϵ_z, however at higher strain, the localization decreases due to increasing ϵ_x and ϵ_y caused the the poisson effect. The conch architecture, though it is made up of layers of oriented lamellae, has slightly decreased localization compared to the homogeneous lamellar architecture, especially at higher strain levels.

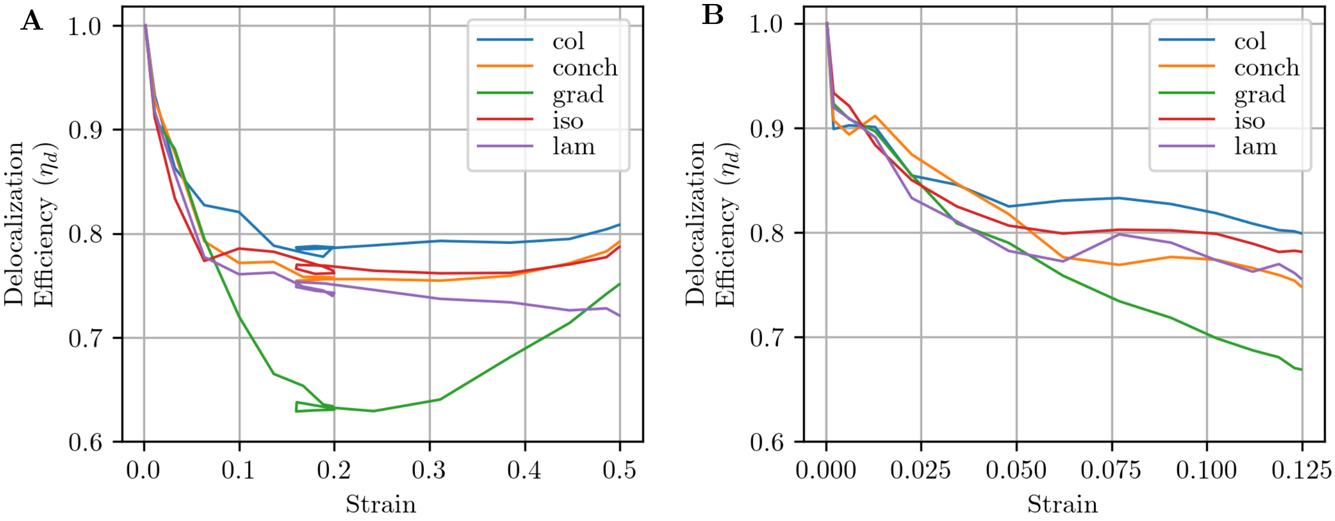

Figure 4.17: Delocalization coefficient as a function of strain. A rapid drop in coefficient to around 0.9 occurs in each plot due to the curved indenter forcing a variation in strain through the structure. (A) 10nm simulations, showing close alignment of the results during the elastic response (until 0.025 strain). After buckling, the results remain largely constant, indicating that no additional localization is occurring. The gradient architecture coefficient increases at high strain due to the poisson effect. (B) 40nm simulations, which show a brief plateau of coefficient prior to buckling. This is not seen in the 10nm plot due to its lower frequency of data outputs.

Chapter 5

SUMMARY AND FUTURE WORK

5.1 Summary

The results of this work have demonstrated a novel understanding of metamaterial behavior by using FEA to inspect a defect-free spinodal nanomaterial. Previous experimental results demonstrated spinodal shell material behavior, but the mixture of architecture and material properties make it difficult to determine the true cause of the behavior seen in the experiment. The simulations used in this study have been validated against the experimental data through the confirmation of the stress-strain curves which show strong correlation with the experimental data in both elastic modulus and plateau stress.

From the comparison of experimental data with the FEA data, it is apparent that the localization of spinodal shells is a result of a combination of real material behavior and manufacturing flaws. The fracture observed in many of the tests lead to significant differences between experiments and simulations. This is especially noticeable after yield, where the simulations show continued hardening, but fracture-prone columnar and isotropic architectures show no hardening, and repeated softening events caused by fracture.Flaws such as shell thickness variation and FIB-induced damage resulted in imperfections which could cause localization due to stress concentrations or premature buckling. This may be applicable to other shell-based nanomaterials, such as TMPS surfaces, since other shell structures are periodic with architectures that are prone to localized collapse. Other variations of spinodal shell materials with different anisotropy, gradients, or feature sizes may also be tested using the same methods, and testing of self-assembled spinodals would be of value to observe the effect of reduced manufacturing defects.

The gradient architectures in this test have shown the ability to control the response and localization properties of the spinodal and spinodoid metamaterials. In particular, the conch architecture showed full recovery and much lower damage than other samples during experimental testing at 40nm. In the FEA results, the conch showed localization of shear strain by layer, but this did not result in diagonal shear bands forming as is often seen in periodic structures. Although the conch outperformed other materials in recovery, its stiffness and plateau stress were also much lower, so the use of this material will depend on the required application. The gradient architecture, with alternating layers of lamellar and columnar structure, showed behavior quite similar to the lamellar layers it contains. As a result, the gradient showed the yield stress and elastic modulus similar to a lamellar structure.

Among spinodal shell materials, architecture has little bearing on the scaling properties, with scaling of modulus ranging from scaling exponent of 1.82 to 1.99 and scaling of yield strength ranging from scaling exponent of 2 to 2.06. Even with different types of anisotropy and gradients, the different architectures show similar features of having large areas of unsupported lamellae which results in an increase in buckling through the structure, which leads to higher scaling exponent. Thus, for future spinodal architectures, we can expect to see similar features and similar behavior.

The stress distribution in each architecture may be inspected in detail using the FEA results, leading to a better understanding of the behavior of each architecture. The architectures have substantial differences in the range of stress values in the structure, indicating that some architectures (columnar, isotropic) may be prone to early failure due to a small number of critical elements which may result in damage propagation in the structure. The conch architecture may experience increased resiliance as the areas of high stress tend to be in areas of connection between lamellae, but if these features were to fail, it would not result in a catastrophic failure or a localized collapse due to the presence of alternate load paths in these locations.

FEA simulations of complex shells such as a spinodal architecture are vulnerable at large displacements to energy losses and persistent self-contact which adversely affects results.

The point at which this problem begins depends on the feature size and architecture design, but it may be seen as the limit to the large strain analysis in FEA for any shell architecture.

5.2 Future Work

The results of this research can be used to inform future work which can provide improvements and resolve unanswered questions.

Further study into the cause of the experimental localization would be useful to try to further understand the differences between the experiments and the simulations. This could include applying a fracture model to the FEA simulations. Ideally, a full damage model for amorphous Alumina would be developed based on experimental validation of its fracture properties. Also, using the curved indenter was useful for validating the FEA to the experimental results, but it may not exactly represent the theoretical properties of the material, and similar simulations should be run without the added curvature.

This research used the S3RS mesh due to its design specifically for Abaqus/Explicit, but it was difficult to verify exactly why its results differed from the S3R mesh. Most similar works use S3R with no explanation, and no comparison of performance and results of the two mesh types could be found, so it may be useful to study the element types more in depth. It would also be useful to develop a 6 node linear strain quadratic element to provide higher accuracy with a lower element count. Currently, 6 node triangular elements are not available in Abaqus/Explicit.

Over the course of this project, it became clear that the original scripts used to clean the meshes needed improvements. For future work using similarly generated meshes it is best to reduce the amount of manual mesh cleaning, so improvements to the mesh cleaning scripts should be made, such as the use of Laplacian smoothing.

Spinodal decomposition shows promise as a method to develop materials, but more work is needed to determine how to control the process to produce a desired architecture. The mechanical properties of self-assembled spinodal materials need to be confirmed in comparison to 3D printed structures.

The results of this work show a path forward to finding optimal spinodal architecture designs, and understanding their performance. The FEA model and scripts used to prepare and process the data may be applied to any other shell architecture, which opens vast possibilities for the exploration of nanoarchitecture properties, especially understanding the fracture mechanisms leading to poor performance of nanomaterials. Ultimately, this research can lead to the design of better architected materials.

Appendix A

SPINODOID STRUCTURES

A.1 Gradient Spinodoid Architectures

The spinodoid architecture is created by using a large number of randomly generated waves to generate a Gaussian Random Field (GRF) which produces a solution similar to the Cahn-Hilliard equation. The positive and negative values of the GRF represent the two phases of the spinodoid structure[19]. The rapid processing time of the spinodoid code allows the generation of the spinodoid structure used in this work in about one minute.

The original spinodoid code is part of the GIBBON open source project[49]. The operation of the spinodoid function is based around generation of a large number of random number vectors which represent a direction in space. When specifying input parameters, three angles θ_i are defined which determine the preferred direction of anisotropy. When the input angles are large, the structure will be more isotropic, and if the angles are small, the structure will be anisotropic. Using the dot product, these are compared to the maximum allowed angles in each primary axis $\hat{\mathbf{e}}_i$, so that if vector $\mathbf{k}$ satisfies one of

$$|\mathbf{k} \cdot \hat{\mathbf{e}}_i| > \cos\theta_i, \text{ for } i = 1, 2, 3 \tag{A.1}$$

the vector will be stored in a list of vectors $\mathbf{n}$, where 1000 vectors were typically generated. This allows an anisotropic selection of vectors to create anisotropic structures. Based on the selection of vectors, a GRF is generated, where the material phase is represented by φ, where

$$\varphi(\mathbf{x}) = \sqrt{\frac{2}{N}} \sum_{i=1}^{N} \cos(\beta \mathbf{n}_i \cdot \mathbf{x} + \gamma_i) \tag{A.2}$$

where N is the number of vectors, β is the wave number chosen in the input parameters, $\mathbf{x}$ represents the location in cartesian space, and γ_i is the randomly generated wave phase. The result is that the directions in which more vectors are found have a shorter wavelength resulting in a smaller feature size compared to other directions.

For this project, the GIBBON spinodoid code was modified to support gradient architectures, based on the November 1, 2020 commit to the GIBBON repository. The spinodoid code defines a unit cell in which a structure is generated, while the revised gradient code defines multiple unit cells along a 1, 2, or 3D grid which each may have different properties. Each unit cell is allowed a certain overlap to the neighboring unit cell over which the values of the GRF are linearly tapered from one unit cell to the next, allowing a smooth transition. In order to support the conch architecture, changes were made to the code, listed below.

- Allowed multiple unit cells in x, y, and z directions, including transitions between unit cells. The values for each unit cell are calculated only for the elements of that unit cell. 3 nested for loops are added to loop through each of the unit cells, and a GRF is generated for each cell in the inside loop.
- Theta values may vary between unit cells.
- Rotation tensor may vary between unit cells. This is done by assigning a rotation tensor for each unit cell, and applying the unique rotation tensor during the generation of wave directions for each unit cell.

The morphology of the isotropic spinodoid models has a strong resemblance to a true spinodal material, allowing it to be a useful stand-in for a spinodal mesh. A lamellar spinodoid has few connections between lamellae, and the connections tend to be highly aligned, due to the use of periodic functions to generate the spinodoid. The lamellar spinodal, in contrast, has more plentiful connections which are stochastically located. The conch architecture described in this work uses eight lamellar unit cells with different orientations. The limitations of the architecture are not obvious in this scale, because the short lamella length does not lead to large unsupported sections.

In the initial phase of this project, prior to the availability of spinodal decomposition data, the compression test videos from Portela et al. were used for experimental data to guide model development, with the 11nm shell thickness isotropic sample used as the baseline, due to its elastic behavior. A spinodoid mesh was generated to match the feature size of the experimental model as closely as possible, and the FEA model used this mesh to test various model parameters, and the stress-strain plots were compared with each iteration.

A.2 Large Gradient Spinodoid Structures

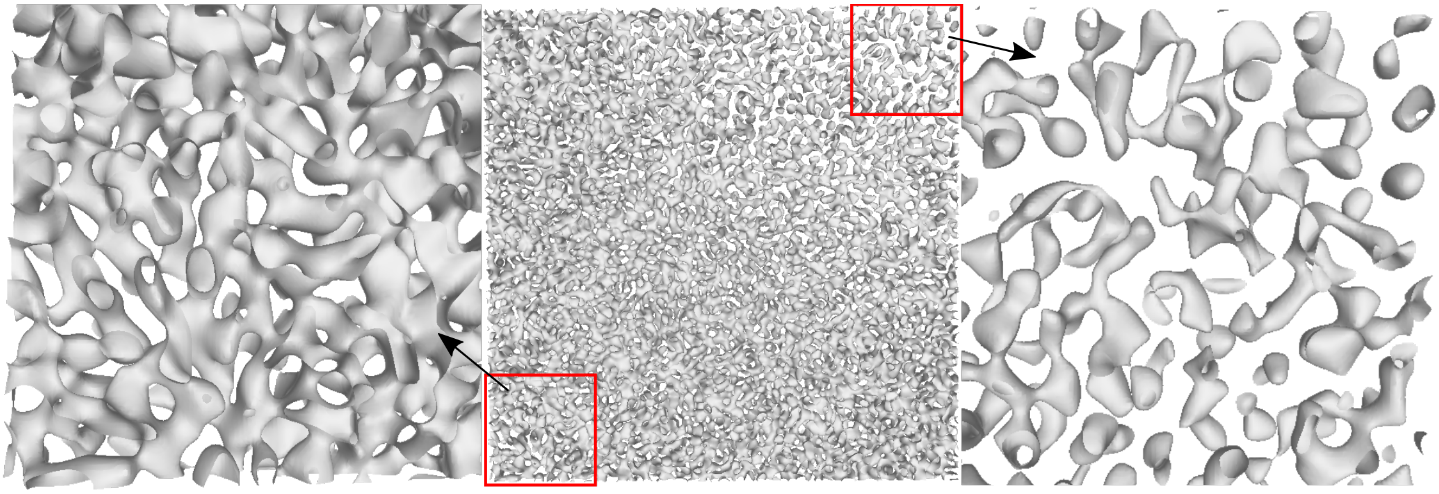

Figure A.1: A portion of the large continuously graded spinodoid mesh, showing 4% of the full mesh. This version does not show the isocaps due to resource constraints. Change in relative density can be seen in the two closeup views.

The use of gradient spinodoid structures in this project was limited to variation in a single dimension, with 8 unit cells. Some of the modifications to the spinodoid code, including gradients of relative density, speed improvements, and status reporting, were added to the code to allow larger scale spinodoid structures to be generated. These changes are listed below, in addition to those described in Section A.1.

- Relative density may vary between unit cells. This is accomplished by changing the levelset (the value of the GRF at which the surface is to be placed) from the isosurface function to the GRF generation. Rather than adjusting the value of the levelset in the isosurface function, the levelset in the isosurface function is set to zero, then the levelset value is added to the GRF for each unit cell. This allows a smooth gradient in relative density between unit cells.
- Added timing and status messages, to help with large gradient structures.
- Various speed related improvements: Keeping only the largest group of faces is disabled by default. Certain mathematical operations have been reordered to make them more efficient. Colors are optional.

The speed of the spinodoid code allows a large number of spinodoid structures to be generated. This enables the use of machine learning to define a spinodoid architecture that matches desired stiffness parameters allowing stochastic structures to be generated to mimic natural materials such as bone[26, 19]. One use of this machine learning model was to create a 100x100 unit cell continuously gradient spinodoid, to allow a continuous gradient of stiffness matrix components. Having the built-in unit cell management allowed efficient operation, and having status logging allowed slow points in the code to be found and improved or disabled.

A structural optimization routine was used to find optimal stiffness values for each of the points in the large grid. These stiffness values were then input into the machine learning model, which produced values for the theta angles and relative density at each grid point, which could then be used as inputs for a spinodoid generation. Using the inputs, the revised 3D spinodoid generation code was able to generate a large mesh, shown in Figure A.1, although the mesh was not used for FEA simulations so it is beyond the scope of this work to discuss the viability of using such a large mesh for analysis.

Appendix B

CYLINDER MESH CONVERGENCE

A cylinder shell with length 0.125mm and diameter of 0.040mm was used as a simplified model to study mesh convergence for shell buckling. The same FEA model parameters were used as with the spinodal tests. A displacement is applied to the cylinder to apply compression and initiate shell buckling. Starting from a mesh seed size of 0.002mm, the seed size was reduced as far as 0.0001mm. The peak reaction force was found for each test, as a measure of mesh convergence.

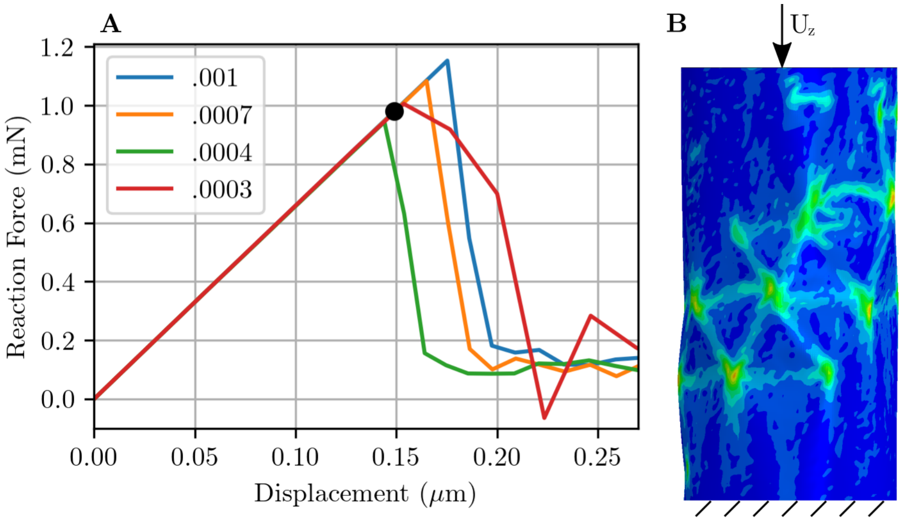

Figure B.1: (A) Mesh convergence of cylinder, showing different mesh seed dimensions. Black dot represents the analytical solution. Both plots represent meshes with S3R elements. (B) The Mises stress in the buckled cylinder at the onset of buckling (bottom of cylinder has been cut off due to no buckling in that area).

A theoretical shell buckling critical load was calculated for the test sample according to the method used by Hilburger [50]. This resulted in a minimum critical buckling load of 0.3155mN. However, this value is based on an empirical factor which assumes some imperfections in the real materials which would always cause a reduction in buckling load. Assuming no knockdown factor, the expected buckling load is 0.9805mN, which is close to the mesh convergence at a buckling load of around 1.0mN, with a 0.0004mm element size. In Figure B.1, this buckling load is plotted against the force-displacement curves of the mesh convergence studies.

Appendix C

DISPLACEMENT AND STRAIN FIELDS

In order to characterize the bulk properties of the spinodal materials, a strain field was calculated based on a sampling of FEA nodal displacements. To simplify output during postprocessing, a subset of nodes is sampled from the mesh and assembled into a node set during preprocessing. The nodes are sampled with a preference for the nodes furthest from the mesh center, with a minimum spacing required between the nodes, in order to include points close to the corners and edges to maximize the usable volume of the interpolation. The target number of sampled nodes is between 1000 and 2000, as too few will have limited data, and too many will slow down postprocessing. This results in an evenly distributed sampling of nodes. The nodal displacement outputs for this node set are used to calculate a detailed displacement field throughout the structure. An interpolation function (scipy LinearNDInterpolator) is created based on these points that can calculate displacement values for any point contained within the interpolation function.

Based on the displacement field, the gradient is calculated to obtain a strain field of all 6 strain tensor components and volumetric strain. The FEA simulation nodal strains were not used to accomplish this because the nodal strains do not take into account the collapse of the gaps between shell surfaces. The strain components are obtained on a regular grid and can be used to determine the overall behavior of the material.

The strain field is demonstrated with the conch architecture, as conch can be expected to have high shear strain when the orientation of lamellae is favorable towards shear strain in a particular direction, leading to alternating high and low strains in the γ_{xz} and γ_{yz} directions. This is shown in Figures 4.8 and 4.11.

The function used to create the displacement and strain fields is shown below. The input file is exported from abaqus, with listings of displacement values in columns labeled with 'Ux', 'Uy', and 'Uz', with each frame in 3 unique columns.

```
def gridValues(filename,modelheight,modelwidth,numGrPt):
  from scipy.interpolate import LinearNDInterpolator
  df = pd.read_csv(filename)
  UxIndex = [i for i,l in enumerate(df.columns.values) if 'Ux' in l]
  UyIndex = [i for i,l in enumerate(df.columns.values) if 'Uy' in l]
  UzIndex = [i for i,l in enumerate(df.columns.values) if 'Uz' in l]
  pt = df[['x','y','z']].to_numpy()

  valuesList = [None]*(len(UxIndex)+1)

  x = np.linspace(min(pt[:,0])+.00001,max(pt[:,0])-.00001,numGrPt)
  y = np.linspace(min(pt[:,1])+.00001,max(pt[:,1])-.00001,numGrPt)
  z = np.linspace(min(pt[:,2])+.00001,max(pt[:,2])-.00001,numGrPt)
  for i in range(len(UxIndex)):
    liUx = LinearNDInterpolator(pt, df.iloc[:,UxIndex[i]])
    liUy = LinearNDInterpolator(pt, df.iloc[:,UyIndex[i]])
    liUz = LinearNDInterpolator(pt, df.iloc[:,UzIndex[i]])

    xGrid,yGrid,zGrid = np.meshgrid(x,y,z,indexing='ij')
    xVec = np.reshape(xGrid,np.size(xGrid))
    yVec = np.reshape(yGrid,np.size(yGrid))
    zVec = np.reshape(zGrid,np.size(zGrid))
    Ux = np.reshape(liUx(list(zip(xVec,yVec,zVec))),np.shape(xGrid))
    Uy = np.reshape(liUy(list(zip(xVec,yVec,zVec))),np.shape(yGrid))
    Uz = np.reshape(liUz(list(zip(xVec,yVec,zVec))),np.shape(zGrid))

    ex = linearStrain2(Ux,xGrid,axis='x')
    ey = linearStrain2(Uy,yGrid,axis='y')
    ez = linearStrain2(Uz,zGrid,axis='z')
    gxy = shearStrain2(Ux,Uy,xGrid,yGrid,'xy')
    gxz = shearStrain2(Ux,Uz,xGrid,zGrid,'xz')
    gyz = shearStrain2(Uy,Uz,yGrid,zGrid,'yz')
    valuesList[i+1] = {'Ux':Ux, 'Uy':Uy, 'Uz':Uz, 'ex':ex, 'ey':ey,
           'ez':ez, 'ev':ex+ey+ez, 'gxz':gxz, 'gyz':gyz, 'gxy':gxy}
  return valuesList

def linearStrain2(ux,x,axis):
  if axis == 1 or axis == '1' or axis=='x':
```

```
    ind = 0
  elif axis == 2 or axis == '2' or axis=='y':
    ind = 1
  elif axis == 3 or axis == '3' or axis=='z':
    ind = 2
  return np.gradient(ux)[ind]/np.gradient(x)[ind]

def shearStrain2(ux1,ux2,x1,x2,axis):
  if axis in [12,21,'12','21','xy','yx']:
    ind = [0,1]
  elif axis in [13,31,'13','31','xz','zx']:
    ind = [0,2]
  elif axis in [23,32,'23','32','yz','zy']:
    ind = [1,2]
  return np.gradient(ux1)[ind[1]]/np.gradient(x2)[ind[1]]
       + np.gradient(ux2)[ind[0]]/np.gradient(x1)[ind[0]]
```

REFERENCES

[1] N. A. Fleck, V. S. Deshpande, and M. F. Ashby. “Micro-architectured materials: past, present and future”. In: *Proceedings of the Royal Society A: Mathematical, Physical and Engineering Sciences* 466.2121 (Sept. 2010), pp. 2495–2516. DOI: `10.1098/rspa.2010.0215`.

[2] T. A. Schaedler, A. J. Jacobsen, A. Torrents, A. E. Sorensen, J. Lian, J. R. Greer, L. Valdevit, and W. B. Carter. “Ultralight metallic microlattices”. In: *Science* 334.6058 (2011), pp. 962–965. DOI: `10.1126/science.1211649`.

[3] Lucas R. Meza, Satyajit Das, and Julia R. Greer. “Strong, lightweight, and recoverable three-dimensional ceramic nanolattices”. In: *Science* 345.6202 (Sept. 2014), pp. 1322–1326. DOI: `10.1126/science.1255908`.

[4] Lucas R. Meza, Alex J. Zelhofer, Nigel Clarke, Arturo J. Mateos, Dennis M. Kochmann, and Julia R. Greer. “Resilient 3D hierarchical architected metamaterials”. In: *Proceedings of the National Academy of Sciences* 112.37 (Sept. 2015), pp. 11502–11507. DOI: `10.1073/pnas.1509120112`.

[5] Xiaoyu Zheng, Howon Lee, Todd H. Weisgraber, Maxim Shusteff, Joshua DeOtte, Eric B. Duoss, Joshua D. Kuntz, Monika M. Biener, Qi Ge, Julie A. Jackson, Sergei O. Kucheyev, Nicholas X. Fang, and Christopher M. Spadaccini. “Ultralight, ultrastiff mechanical metamaterials”. In: *Science* 344.6190 (2014), pp. 1373–1377. DOI: `10.1126/science.1252291`.

[6] J. Bauer, A. Schroer, R. Schwaiger, and O. Kraft. “Approaching theoretical strength in glassy carbon nanolattices”. In: *Nature Materials* 15.4 (Apr. 2016), pp. 438–443. DOI: `10.1038/nmat4561`.

[7] X. Wendy Gu and Julia R. Greer. “Ultra-strong architected Cu meso-lattices”. In: *Extreme Mechanics Letters* 2.1 (Mar. 2015), pp. 7–14. DOI: `10.1016/j.eml.2015.01.006`.

[8] Carlos M. Portela, Bryce W. Edwards, David Veysset, Yuchen Sun, Keith A. Nelson, Dennis M. Kochmann, and Julia R. Greer. “Supersonic impact resilience of nanoarchitected carbon”. In: *Nature Materials* 20.11 (Nov. 2021), pp. 1491–1497. DOI: `10.1038/s41563-021-01033-z`.

[9] Jens Bauer, Lucas R. Meza, Tobias A. Schaedler, Ruth Schwaiger, Xiaoyu Zheng, and Lorenzo Valdevit. “Nanolattices: An Emerging Class of Mechanical Metamaterials”. In: *Advanced Materials* 29.40 (Oct. 2017), p. 1701850. DOI: `10.1002/adma.201701850`.

[10] Lorenzo Valdevit, Scott W. Godfrey, Tobias A. Schaedler, Alan J. Jacobsen, and William B. Carter. “Compressive strength of hollow microlattices: Experimental characterization, modeling, and optimal design”. In: *Journal of Materials Research* 28.17 (2013), pp. 2461–2473. DOI: `10.1557/jmr.2013.160`.

[11] Stephen Timoshenko and S Woinowsky-Krieger. *Theory of plates and shells*. New York: McGraw-Hill, 1959, p. 580.

[12] Alan H. Schoen. *Infinite Periodic Minimal Surfaces Without Self-Intersections*. Tech. rep. Cambridge, MA: NASA, 1970.

[13] Yunfei Zhang, Meng Ting Hsieh, and Lorenzo Valdevit. “Mechanical performance of 3D printed interpenetrating phase composites with spinodal topologies”. In: *Composite Structures* 263.August 2020 (2021), p. 113693. DOI: `10.1016/j.compstruct.2021.113693`.

[14] V. Pini, J. J. Ruz, P. M. Kosaka, O. Malvar, M. Calleja, and J. Tamayo. “How two-dimensional bending can extraordinarily stiffen thin sheets”. In: *Scientific Reports* 6.1 (July 2016), p. 29627. DOI: `10.1038/srep29627`.

[15] Carlos M. Portela, A. Vidyasagar, Sebastian Krödel, Tamara Weissenbach, Daryl W. Yee, Julia R. Greer, and Dennis M. Kochmann. "Extreme mechanical resilience of self-assembled nanolabyrinthine materials". In: *Proceedings of the National Academy of Sciences* 117.11 (Mar. 2020), pp. 5686–5693. DOI: `10.1073/pnas.1916817117`.

[16] Colin Bonatti and Dirk Mohr. "Mechanical performance of additively-manufactured anisotropic and isotropic smooth shell-lattice materials: Simulations & experiments". In: *Journal of the Mechanics and Physics of Solids* 122 (2019), pp. 1–26. DOI: `10.1016/j.jmps.2018.08.022`.

[17] Colin Bonatti and Dirk Mohr. "Smooth-shell metamaterials of cubic symmetry: Anisotropic elasticity, yield strength and specific energy absorption". In: *Acta Materialia* 164 (2019), pp. 301–321. DOI: `10.1016/j.actamat.2018.10.034`.

[18] Seung Chul Han, Jeong Myung Choi, Gang Liu, and Kiju Kang. "A Microscopic Shell Structure with Schwarz's D-Surface". In: *Scientific Reports* 7.1 (Oct. 2017), p. 13405. DOI: `10.1038/s41598-017-13618-3`.

[19] Siddhant Kumar, Stephanie Tan, Li Zheng, and Dennis M. Kochmann. "Inverse-designed spinodoid metamaterials". In: *npj Computational Materials* 6.1 (Dec. 2020), p. 73. DOI: `10.1038/s41524-020-0341-6`.

[20] Meng-Ting Hsieh, Bianca Endo, Yunfei Zhang, Jens Bauer, and Lorenzo Valdevit. "The mechanical response of cellular materials with spinodal topologies". In: *Journal of the Mechanics and Physics of Solids* 125 (Apr. 2019), pp. 401–419. DOI: `10.1016/j.jmps.2019.01.002`.

[21] Anna Guell Izard, Jens Bauer, Cameron Crook, Vladyslav Turlo, and Lorenzo Valdevit. "Ultrahigh Energy Absorption Multifunctional Spinodal Nanoarchitectures". In: *Small* 15.45 (Nov. 2019), p. 1903834. DOI: `10.1002/smll.201903834`.

[22] John W. Cahn. "On spinodal decomposition". In: *Acta Metallurgica* 9.9 (Sept. 1961), pp. 795–801. DOI: `10.1016/0001-6160(61)90182-1`.

[23] John W. Cahn. “Phase Separation by Spinodal Decomposition in Isotropic Systems”. In: *The Journal of Chemical Physics* 42.1 (Jan. 1965), pp. 93–99. DOI: `10.1063/1.1695731`.

[24] C. L. Park, J. W. Gibbs, P. W. Voorhees, and K. Thornton. “Coarsening of complex microstructures following spinodal decomposition”. In: *Acta Materialia* 132 (2017), pp. 13–24. DOI: `10.1016/j.actamat.2017.03.020`.

[25] A. Vidyasagar, S. Krödel, and D. M. Kochmann. “Microstructural patterns with tunable mechanical anisotropy obtained by simulating anisotropic spinodal decomposition”. In: *Proceedings of the Royal Society A: Mathematical, Physical and Engineering Sciences* 474.2218 (Oct. 2018), p. 20180535. DOI: `10.1098/rspa.2018.0535`.

[26] Li Zheng, Siddhant Kumar, and Dennis M. Kochmann. “Data-driven topology optimization of spinodoid metamaterials with seamlessly tunable anisotropy”. In: *Computer Methods in Applied Mechanics and Engineering* 383 (Sept. 2021), p. 113894. DOI: `10.1016/j.cma.2021.113894`.

[27] Norio Tsujioka, Norio Ishizuka, Nobuo Tanaka, Takuya Kubo, and Ken Hosoya. “Well-controlled 3D skeletal epoxy-based monoliths obtained by polymerization induced phase separation”. In: *Journal of Polymer Science Part A: Polymer Chemistry* 46.10 (May 2008), pp. 3272–3281. DOI: `10.1002/pola.22665`.

[28] Jens Bauer, Julie A Kraus, Cameron Crook, Julian J Rimoli, and Lorenzo Valdevit. “Tensegrity Metamaterials: Toward Failure-Resistant Engineering Systems through Delocalized Deformation”. In: *Advanced Materials* 33.10 (Mar. 2021), p. 2005647. DOI: `10.1002/adma.202005647`.

[29] M.F Ashby. “The properties of foams and lattices”. In: *Philosophical Transactions of the Royal Society A: Mathematical, Physical and Engineering Sciences* 364.1838 (Jan. 2006), pp. 15–30. DOI: `10.1098/rsta.2005.1678`.

[30] Shelby B. Hutchens, Alan Needleman, and Julia R. Greer. "A microstructurally motivated description of the deformation of vertically aligned carbon nanotube structures". In: *Applied Physics Letters* 100.12 (Mar. 2012), p. 121910. DOI: `10.1063/1.3697686`.

[31] Alan Needleman, Shelby B. Hutchens, N. Mohan, and J. R. Greer. "Deformation of plastically compressible hardening-softening-hardening solids". In: *Acta Mechanica Sinica* 28.4 (Aug. 2012), pp. 1115–1124. DOI: `10.1007/s10409-012-0117-4`.

[32] Hao Wu, Juzheng Chen, Ke Duan, Mengya Zhu, Yuan Hou, Jingzhuo Zhou, Yukun Ren, Hongyuan Jiang, Rong Fan, and Yang Lu. "Three Dimensional Printing of Bioinspired Crossed-Lamellar Metamaterials with Superior Toughness for Syntactic Foam Substitution". In: *ACS Applied Materials & Interfaces* 14.37 (Sept. 2022), pp. 42504–42512. DOI: `10.1021/acsami.2c12297`.

[33] Dongchan Jang, Lucas R. Meza, Frank Greer, and Julia R. Greer. "Fabrication and deformation of three-dimensional hollow ceramic nanostructures". In: *Nature Materials* 12.10 (Oct. 2013), pp. 893–898. DOI: `10.1038/nmat3738`.

[34] L. T. Kuhn-Spearing, H. Kessler, E. Chateau, R. Ballarini, A. H. Heuer, and S. M. Spearing. "Fracture mechanisms of the Strombus gigas conch shell: Implications for the design of brittle laminates". In: *Journal of Materials Science* 31.24 (1996), pp. 6583–6594. DOI: `10.1007/BF00356266`.

[35] Grace X. Gu, Mahdi Takaffoli, and Markus J. Buehler. "Hierarchically Enhanced Impact Resistance of Bioinspired Composites". In: *Advanced Materials* 29.28 (2017), pp. 1–7. DOI: `10.1002/adma.201700060`.

[36] Joseph Cadman, Shiwei Zhou, Yuhang Chen, Wei Li, Richard Appleyard, and Qing Li. "Characterization of cuttlebone for a biomimetic design of cellular structures". In: *Acta Mechanica Sinica* 26.1 (Mar. 2010), pp. 27–35. DOI: `10.1007/s10409-009-0310-2`.

[37] J. D. Birchall and N. L. Thomas. "On the architecture and function of cuttlefish bone". In: *Journal of Materials Science* 18.7 (July 1983), pp. 2081–2086. DOI: `10.1007/BF00555001`.

[38] S. Kannan, J. H.G. Rocha, S. Agathopoulos, and J. M.F. Ferreira. "Fluorine-substituted hydroxyapatite scaffolds hydrothermally grown from aragonitic cuttlefish bones". In: *Acta Biomaterialia* 3.2 (2007), pp. 243–249. DOI: `10.1016/j.actbio.2006.09.006`.

[39] Z. Hashin and S. Shtrikman. "A variational approach to the theory of the elastic behaviour of multiphase materials". In: *Journal of the Mechanics and Physics of Solids* 11.2 (Mar. 1963), pp. 127–140. DOI: `10.1016/0022-5096(63)90060-7`.

[40] Lucas R Meza, Gregory P Phlipot, Carlos M Portela, Alessandro Maggi, Lauren C Montemayor, Andre Comella, Dennis M Kochmann, and Julia R Greer. "Reexamining the mechanical property space of three-dimensional lattice architectures". In: *Acta Materialia* 140 (Nov. 2017), pp. 424–432. DOI: `10.1016/j.actamat.2017.08.052`.

[41] Hang-Shing Ma, Jean-H Prévost, Rémi Jullien, and George W. Scherer. "Computer simulation of mechanical structure–property relationship of aerogels". In: *Journal of Non-Crystalline Solids* 285.1-3 (June 2001), pp. 216–221. DOI: `10.1016/S0022-3093(01)00456-2`.

[42] Maria Berdova, Tuomo Ylitalo, Ivan Kassamakov, Jouni Heino, Pekka T. Törmä, Lauri Kilpi, Helena Ronkainen, Jari Koskinen, Edward Hæggström, and Sami Franssila. "Mechanical assessment of suspended ALD thin films by bulge and shaft-loading techniques". In: *Acta Materialia* 66 (2014), pp. 370–377. DOI: `10.1016/j.actamat.2013.11.024`.

[43] Kari Koski, Jorma Hölsä, and Pierre Juliet. "Properties of aluminium oxide thin films deposited by reactive magnetron sputtering". In: *Thin Solid Films* 339.1-2 (1999), pp. 240–248. DOI: `10.1016/S0040-6090(98)01232-2`.

[44] *Abaqus Theory Guide R2022x*. 2022.

[45] Richard H. Macneal. “Derivation of element stiffness matrices by assumed strain distributions”. In: *Nuclear Engineering and Design* 70.1 (June 1982), pp. 3–12. DOI: `10.1016/0029-5493(82)90262-X`.

[46] J. M. Kennedy, T. Belytschko, and J. I. Lin. “Recent developments in explicit finite element techniques and their application to reactor structures”. In: *Nuclear Engineering and Design* 97.1 (1986), pp. 1–24. DOI: `10.1016/0029-5493(86)90067-1`.

[47] Keunhwan Pack and Dirk Mohr. “Combined necking & fracture model to predict ductile failure with shell finite elements”. In: *Engineering Fracture Mechanics* 182 (Sept. 2017), pp. 32–51. DOI: `10.1016/j.engfracmech.2017.06.025`.

[48] Jens Bauer, Almut Schroer, Ruth Schwaiger, Iwiza Tesari, Christian Lange, Lorenzo Valdevit, and Oliver Kraft. “Push-to-pull tensile testing of ultra-strong nanoscale ceramic–polymer composites made by additive manufacturing”. In: *Extreme Mechanics Letters* 3 (June 2015), pp. 105–112. DOI: `10.1016/j.eml.2015.03.006`.

[49] Kevin M Moerman. “GIBBON: The Geometry and Image-Based Bioengineering add-On”. In: *The Journal of Open Source Software* 3.22 (Feb. 2018), p. 506. DOI: `10.21105/joss.00506`.

[50] Mark W Hilburger. *Buckling of thin-walled circular cylinders.* Tech. rep. December 2020. Hampton, Virginia: NASA Langley Research Center, 2020.